



**HAL**  
open science

# Strong Shaking Predicted in Tokyo From an Expected M7+ Itoigawa-Shizuoka Earthquake

Marine A. Denolle, Pierre Boué, Naoshi Hirata, Gregory C. Beroza

► **To cite this version:**

Marine A. Denolle, Pierre Boué, Naoshi Hirata, Gregory C. Beroza. Strong Shaking Predicted in Tokyo From an Expected M7+ Itoigawa-Shizuoka Earthquake. *Journal of Geophysical Research: Solid Earth*, 2018, 123, pp.3968-3992. 10.1029/2017JB015184 . insu-03595909

**HAL Id: insu-03595909**

**<https://insu.hal.science/insu-03595909>**

Submitted on 3 Mar 2022

**HAL** is a multi-disciplinary open access archive for the deposit and dissemination of scientific research documents, whether they are published or not. The documents may come from teaching and research institutions in France or abroad, or from public or private research centers.

L'archive ouverte pluridisciplinaire **HAL**, est destinée au dépôt et à la diffusion de documents scientifiques de niveau recherche, publiés ou non, émanant des établissements d'enseignement et de recherche français ou étrangers, des laboratoires publics ou privés.

Copyright

## RESEARCH ARTICLE

10.1029/2017JB015184

# Strong Shaking Predicted in Tokyo From an Expected M7+ Itoigawa-Shizuoka Earthquake

 Marine A. Denolle<sup>1</sup> , Pierre Boué<sup>2</sup> , Naoshi Hirata<sup>3</sup>, and Gregory C. Beroza<sup>4</sup> 

<sup>1</sup>Department of Earth and Planetary Sciences, Harvard University, Cambridge, MA, USA, <sup>2</sup>Institut des Sciences de la Terre, CNRS, Université Grenoble Alpes, Grenoble, France, <sup>3</sup>Earthquake Research Institute, University of Tokyo, Tokyo, Japan, <sup>4</sup>Department of Geophysics, Stanford University, Stanford, CA, USA

**Key Points:**

- Ambient-field Green's function allows us to reliably predict shaking of future earthquakes
- Long-range wave propagation controls ground motion strength and variability
- Tokyo will experience strong shaking in the next crustal earthquakes

**Supporting Information:**

- Supporting Information S1

**Correspondence to:**
 M. A. Denolle,  
 mdenolle@fas.harvard.edu
**Citation:**

Denolle, M. A., Boué, P., Hirata, N., & Beroza, G. C. (2018). Strong shaking predicted in Tokyo from an expected M7+ Itoigawa-Shizuoka earthquake. *Journal of Geophysical Research: Solid Earth*, 123, 3968–3992. <https://doi.org/10.1029/2017JB015184>

Received 2 NOV 2017

Accepted 4 APR 2018

Accepted article online 27 APR 2018

Published online 12 MAY 2018

**Abstract** The Itoigawa-Shizuoka Tectonic Line (ISTL) is a major oblique left-lateral crustal fault that is expected to host M7+ events in the near future. Its proximity to the Kanto sedimentary basin poses a threat to the population of Metropolitan Tokyo. This study constructs ground motion predictions for scenario earthquakes on the ISTL using virtual earthquakes. We use the ambient seismic field to calculate the cross-correlation function that we assume proportional to the elastodynamic Green tensor between High-Sensitivity Seismograph network stations, which act as sources located above the ISTL, and the stations of the dense Metropolitan Seismic Observation network, which act as receivers in the Kanto Basin. We use the virtual earthquake approach (Denolle et al., 2013, <https://doi.org/10.1029/2012JB009603>; Denolle, Dunham, et al., 2014, <https://doi.org/10.1126/science.1245678>) to predict ground motion from a suite of 270 kinematic sources and find that predicted ground motions are strong enough that nonlinear effects, which we do not model, may become important. We find that the shape of the sedimentary basin substantially alters the shaking by amplifying long-period ground motions as seismic waves refract at the basin edge. Additionally, we quantify ground motion variability due to source uncertainty, surmise that ground motions are lognormally distributed with regard to source uncertainties, and suggest that the variability is affected (locally either enhanced or reduced) by the basin shape. Finally, we find a coupling point between source and wave paths for epicentral locations on the ISTL that generates almost twice the shaking as equivalent unilateral ruptures, despite directivity orientation that would favor southward ruptures.

**Plain Language Summary** The Itoigawa-Shizuoka Tectonic Line (ISTL) is a major crustal fault that is expected to host M7+ events in the future. Its proximity to the Kanto sedimentary basin poses a threat to the population of Metropolitan Tokyo. This study constructs ground motion predictions for scenario earthquakes on the ISTL using continuous recordings of the ambient seismic field. It takes advantage of dense seismic networks in Japan (High-Sensitivity Seismograph network and Metropolitan Seismic Observation network) to characterize seismic wave propagation in complex sedimentary basin structures. The results show that the sedimentary basin shape particularly affects the strength of the ground shaking and its variability. Overall, ground motion levels for a future ISTL earthquake are large and likely to affect tall infrastructures such as tall buildings and bridges.

## 1. Introduction

The Tokyo Metropolitan area is subject to high earthquake activity due to its location near the complex junction of three plates. More than 26 million inhabitants and critically important Japanese infrastructures are exposed to high seismic risk. The M7.9 Great Kanto earthquake struck Tokyo in 1923, caused more than 120,000 fatalities, and was a subduction zone earthquake located underneath Tokyo-Yokohama. The M8 Mino-Owari earthquake, also in Central Honshu in 1891, was a crustal earthquake and had a maximum surface offset of 8 m and a surface rupture of 80 km (Fukuyama & Mikumo, 2006) that caused damage in Osaka and Nagoya and was felt as far as Tokyo. Both subduction zone earthquakes and crustal earthquakes carry potential for extensive damage in Honshu.

The Itoigawa-Shizuoka Tectonic Line (ISTL) is among the crustal fault zones that comprise the three plate boundaries and that are capable of hosting large M7+ earthquakes (Okumura et al., 1994). It extends across

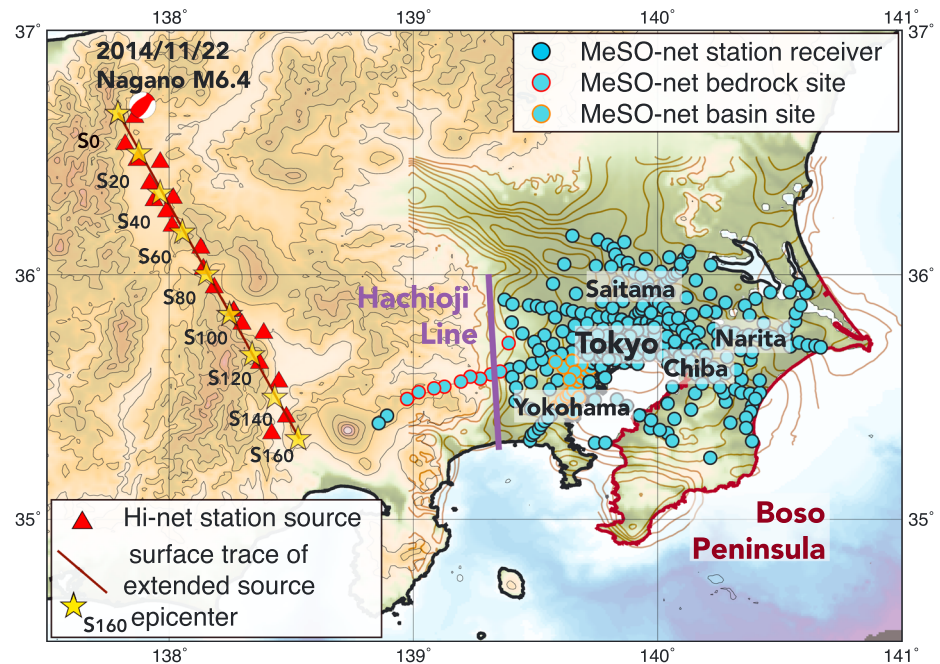


**Figure 1.** Map showing MeSO-net stations (cyan circles), Hachioji Line (purple line), and Hi-net stations used as virtual sources (red triangles). Epicentral locations used in this study are indicated by the yellow stars. Major cities are marked by their name; the Boso Peninsular is contoured by its coastline in brown. The M6.2 Northern Nagano earthquake is shown with its focal mechanism (National Research Institute for Earth Science and Disaster solution). Topography is shown in colorscale and extracted from [topex.ucsd.edu](http://topex.ucsd.edu) (Smith & Sandwell, 1997), and basin contours are the iso  $V_S = 3.2$ -km/s contours (Koketsu et al., 2009). Hi-net = High-Sensitivity Seismograph network; MeSO-net = Metropolitan Seismic Observation network.

Honshu as a north-south feature that separates the island into southwestern and northeastern blocks, at the southern edge of the rift zone that opened the Sea of Japan (H. Sato, 1994). The faulting mechanism of the ISTL varies along strike; it transitions from predominantly thrust motion in the north to predominantly strike-slip motion in the south (Kondo et al., 2006; Sagiya et al., 2004). The ISTL is segmented but has hosted magnitude 7–8 earthquakes in the past; the largest single-event slip measured at the surface is 6–9 m, and the ISTL is thought to have recurrence times of about 1,000 years (Okumura, 2001; Okumura et al., 1994). The last significant earthquake was in CE 841, and no earthquake of magnitude 7 or greater has occurred in the last 1,200 years. The ISTL is thought to be at a mature stage of its cycle with a probability of occurrence on its northern segment of 22% by 2047 (Japan Seismic Hazard Information Station). The M6.2, 22 November 2014, Northern Nagano earthquake ruptured the Kamishiro Thrust, which is the northern active segment of the ISTL and was well recorded in Kanto Basin by the dense array of 296 shallow boreholes accelerometers, the Metropolitan Seismic Observation network (MeSO-net).

The ISTL is only 100–200 km away from greater Tokyo, and the seismic hazard Tokyo faces from it is increased by the presence of the Kanto sedimentary basin. The Kanto sedimentary basin is a deep basin with a basement depth as deep as 4 km (Afnimar et al., 2003; Koketsu et al., 2009). Complex sedimentary basin structures present particular challenges to seismic hazard assessment as they trap seismic waves, amplifying the shaking and extending its duration (Kawase & Aki, 1989). Seismic amplification occurs because soft sediments have a lower seismic wave speed than surrounding bedrock. Seismic amplification is strongest around 6- to 7-s period in Kanto (Denolle, Miyake, et al., 2014; Furumura & Hayakawa, 2007; Miyake & Koketsu, 2005; T. Sato et al., 1990). The low wave speed sediments also promote the excitation of high-frequency surface waves (Tsai et al., 2017) and higher-mode surface waves (Bard & Bouchon, 1980; Boué et al., 2016; Cruz-Atienza et al., 2016; Kawase & Aki, 1989), which greatly extends the duration of shaking. The trapping of seismic waves can be explained by wave focusing with refraction (Koketsu & Kikuchi, 2000) and reflection (Boué et al., 2016) along or at the western basin edge, referred to as the Hachioji Line (see Figure 1).

**Table 1**  
*Virtual Source Stations From Hi-Net*

Station name	Latitude (°)	Longitude (°)	Distance from fault trace (km)
HKKH	36.53	137.8201	6.6
OM2H	36.37	1137.9203	17.5
AAKH	36.53	137.9390	4.0
ATYH	36.4598	137.9637	20.5
IKSH	36.5533	137.9415	14.9
MANH	36.3127	138.0167	3.3
MMOH	36.2578	137.9898	3.8
MNYH	36.1987	138.0122	6.9
SSWH	36.1088	138.1297	4.7
SSGH	36.0233	138.1400	4.6
CHNH	35.9465	138.1848	6.7
HQNH	35.8501	138.2644	5.8
HQSH	35.7974	138.2982	9.7
NRSH	35.7604	138.3874	8.5
OMYH	36.4680	137.8692	5.7

Note. Hi-Net = High-Sensitivity Seismograph network.

Predicting ground motion accurately is critical to assessing and mitigating seismic risk. The conventional approach to predicting ground motion is through empirical relations that express the shaking level as a function of source and path properties based on shaking intensity measurements of past earthquakes. These ground motion prediction equations (Douglas & Edwards, 2016) suffer from the lack of data for large earthquakes at close distances. To remedy this shortage of data, numerical simulations of wave propagation in three-dimensional models of Earth structure allow a theoretical prediction of ground motion, provided that we know the accuracy and the uncertainty of the models (Day et al., 2012; Graves et al., 2011; Olsen et al., 2006, 2009; Roten et al., 2014). Interestingly, the disagreement between those two approaches to ground motion predictions is strongest at long periods (5–10 s; Wang & Jordan, 2014).

Prieto and Beroza (2008) proposed to use the cross correlation of the ambient seismic field simultaneously recorded at seismic stations to retrieve empirically 3-D elastic and anelastic path effects. The interpretation of the seismic amplitudes in terms of scattering and intrinsic attenuation has been widely discussed (Bowden et al., 2016; Lawrence & Prieto, 2011; Lawrence et al., 2013; Prieto et al., 2009). Viens et al. (2017) have shown that seismic amplitudes obtained from the deconvolution of the ambient seismic field reliably reproduced those observed during earthquakes using similar data and in the Kanto Basin. Denolle et al. (2013) built from this concept and developed the virtual earthquake approach (VEA) that takes those cross correlations and turns them into waveforms from buried double-couple point sources. Denolle, Dunham, et al. (2014) extended the VEA point-source method to reproduce the finite-fault effects of large kinematic ruptures and applied it to predict long period (4–10 s) shaking from a future San Andreas earthquake in the Los Angeles Basin.

Here we follow Denolle, Dunham, et al. (2014) and construct a suite of scenario earthquakes on the ISTL to predict the shaking in the sediments of the Kanto Basin and in particular in metropolitan Tokyo. We construct pseudo-dynamic source models (Crempien & Archuleta, 2015; Guatteri et al., 2003; Schmedes et al., 2010) of a planar oblique left-lateral fault. We take advantage of the dense seismic network MeSO-net (Figure 1) and of the locations of the Hi-net (High-Sensitivity Seismograph network; Figure 1 and Table 1) stations near the ISTL fault to build virtual earthquakes from the ambient seismic field. First, we construct the Earth's impulse response from deconvolution of the ambient seismic field recorded between Hi-net stations (as sources) and MeSO-net stations (as receivers) with a method that preserves the relative amplitudes of the response (Denolle et al., 2013; Prieto & Beroza, 2008). To calibrate the relative amplitudes to absolute levels, we adjust the VEA predictions to fit the observed shaking in Kanto from the 2014 Northern Nagano earthquake. The VEA waveforms are practically the convolution of a synthetic source term and an empirical 3-D Green's function.

We then discuss the cross-correlation results, which unsurprisingly bear similarities to the findings of Boué et al. (2016). Both of our studies find that wave propagation from outside to within the sedimentary basin

exhibit strong excitation of the first overtone mode at the basin edge. We elaborate on the source models and waveform synthetics constructed in laterally homogeneous medium to offer a discussion between ground motions from a simple and from a realistic 3-D medium. Calibration of the relative VEA amplitudes to absolute levels is performed using the Nagano earthquake. Finally, we examine and interpret our results for larger scenario earthquakes for both waveform predictions from the VEA and from the laterally homogeneous medium. We show that the predicted long-period (1–10 s) ground motion is high enough to trigger nonlinear effects. We find that crustal structure couples with source effects, whereby ground motion variability is either enhanced or reduced with 3-D crustal structure as opposed to ground motions from laterally homogeneous media. We also highlight a given epicentral location in the Matsumoto Basin where the coupling of source and wave propagation yield particular strong ground motion effects.

## 2. Ambient Seismic Field Green's Function

We construct the impulse response function through a deconvolution technique that has been shown to preserve the relative amplitudes of the Green's function (Denolle et al., 2013; Prieto & Beroza, 2008; Prieto et al., 2011). The nine possible deconvolution functions form what we refer to as the Green tensor. The cross-correlation (or deconvolution) functions are approximately proportional to the elastodynamic Green tensor under appropriate conditions on the noise wavefield (Sánchez-Sesma & Campillo, 2006; Stehly et al., 2006). The virtual source stations are listed in Table 1. Hi-net stations (virtual sources) are short-period velocimeters that sample the wavefield at 100 Hz and the MeSO-net stations (receivers) are accelerometers that sample the wavefield at 200 Hz. We low-pass filter to 2.5 Hz and downsample all raw seismograms to 20 Hz, cut the time series into 30-min time windows overlapped by 50% (Seats et al., 2011), remove their means and trends, ignore those with absolute amplitudes exceeding 10 times the window standard deviation to remove the transient signals and perform the deconvolution in frequency domain. The displacement Green's function between the virtual source  $A$  and the receiver  $B$ ,  $G^{AB}(t)$  is proportional to the first time derivative of the deconvolution function. Given the nine components of the Green tensor,  $i, j \in [1, 3]$ , the deconvolution of the seismograms at the virtual source  $u_i^A(t)$  and the receiver  $u_j^B(t)$  yields in the frequency domain:

$$\widehat{G}_{ij}^{AB}(\omega) = i\omega C \left\langle \frac{\hat{u}_i^B(\omega)\hat{u}_j^{A*}(\omega)}{\{|\hat{u}_j^A(\omega)|\}^2} \right\rangle, \quad (1)$$

where the operator  $\langle \rangle$  denotes stacking over time windows and  $\{ \}$  denotes smoothing over the virtual source spectrum (15-point running average) to ensure stability in the deconvolution. The factor  $C$  is a scalar that depends on the energies of diffuse P and S waves (Sánchez-Sesma & Campillo, 2006) and that is effectively common to all stations, provided that the station pairs are subject to the same seismic noise, which is appropriate for regional-scale study. We stack each deconvolution function over the 3-year period, from January 2010 to December 2012. For computational efficiency and because the instrumental response of both Hi-net instruments and MeSO-net instruments has not significantly changed over the course of 3 years, we remove the responses on the final stack in the frequency domain. We remove the mean of the spectrum and perform an inverse Fourier transform to return to the time domain. Finally, we rotate the tensor from the north-east-down coordinate system to the radial-transverse-down coordinate system assuming a straight-line raypath between the virtual source and receiver and take the convention that the radial component is positive outward from the source-receiver axis. The VEA treats the surface-wave modes separately such that the rotation of the Green tensor is necessary to isolate the modes of Rayleigh and Love waves.

The cross-correlation functions are predominantly anticausal on all nine components of the Green tensor (see Figures S1 and S3 in the supporting information), indicating that the ambient seismic field is mainly excited in the Pacific Ocean rather than the Japan Sea. Their asymmetry is more pronounced for the receiver vertical components ZZ, RZ, and TZ (see Figures S2, S4, and S5) and does not appear to vary with azimuth as all of the virtual sources have a similar degree of asymmetry (Figure S5). At each virtual source, the azimuthal variations of the amplitudes, at all components, are dominated by basin amplification (Figure S6), and thus, an uneven distribution of noise sources does not dominate the signal (Stehly & Boué, 2017; Stehly et al., 2006; Yao et al., 2009). Thus, we assume an even distribution of noise sources in the considered range of azimuths, limiting possible biases on relative amplitude estimates. We average both sides of the Green's function as in Denolle et al. (2013) and Denolle, Dunham, et al. (2014).

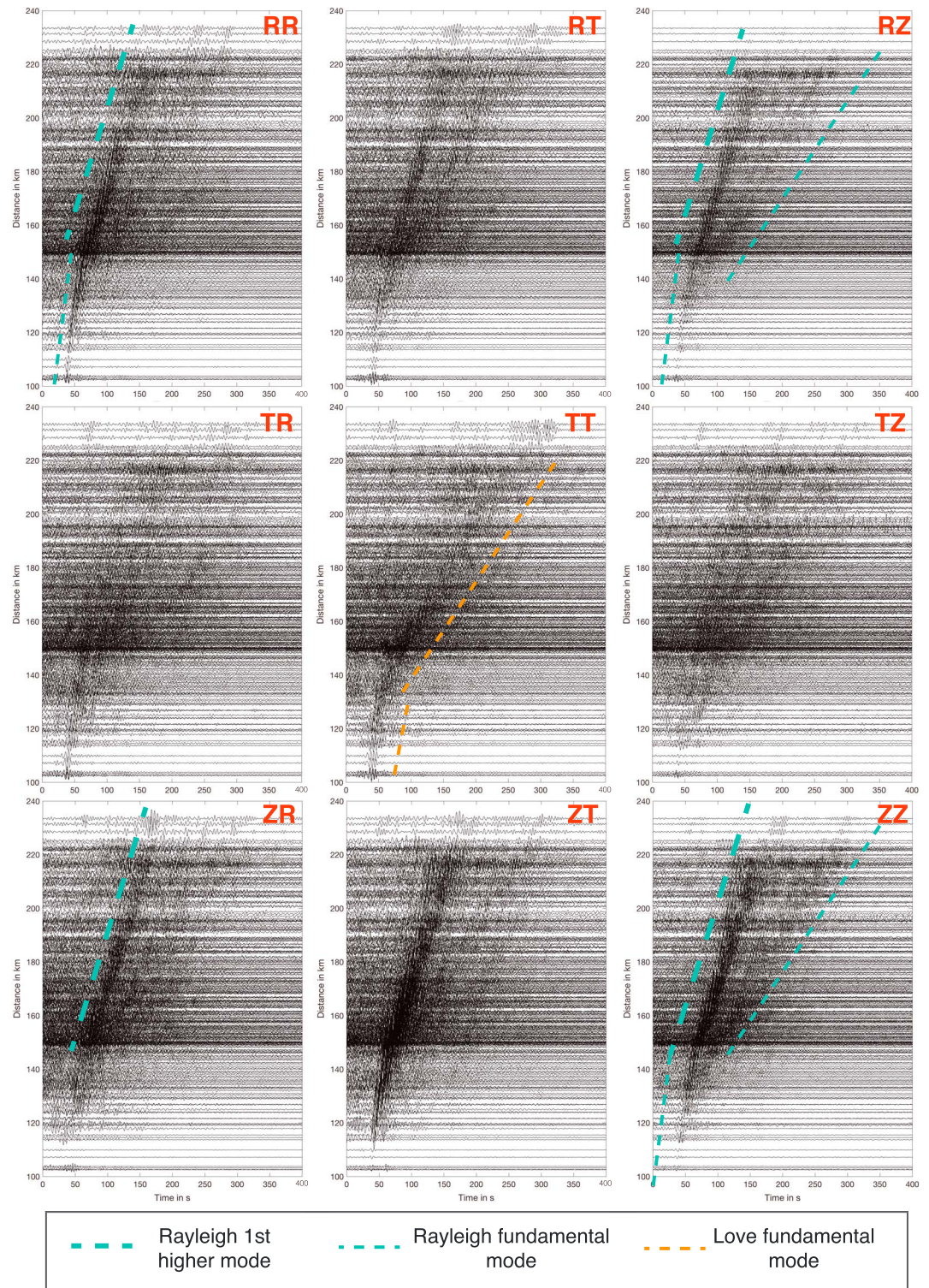


**Figure 2.** Averaged cross-correlation functions from virtual source SSWH to all Metropolitan Seismic Observation network stations and at all nine components of the Green tensor. The dash colored lines provide a crude indication of the move out of Love and Rayleigh wave fundamental modes and Rayleigh wave first higher modes.

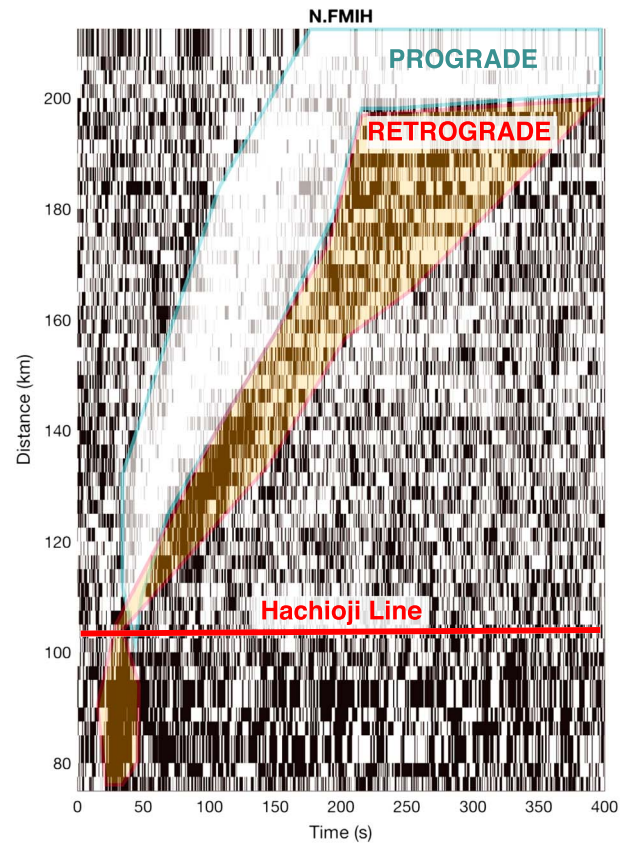


**Figure 3.** Polarization function with distance from the virtual source FMIH. Black color refers to a retrograde polarization, and white refers to a prograde polarization. The Hachioji Line (Figure 2) defines the sharp boundary between bedrock and basin sediments beyond which wave speed greatly decreases and the prograde higher mode becomes prominent. The retrograde particle motion is interpreted as characteristic of the fundamental mode in the 1- to 10-s band, whereas the prograde particle motion is characteristic of the first overtone (Boué et al., 2016). The polarization function suggests that the fundamental mode also has a prograde particle motion at the greatest distances, which is expected given the velocity profile and the frequency band (Figure 5 of Boué et al., 2016).

### 2.1. Fundamental and First Higher Modes

Figure 2 shows the nine components of the Green tensor for virtual source SSWH. Both Viens et al. (2016) and Boué et al. (2016) analyzed the content of the waveforms and concluded that surface waves dominate the signal. The Rayleigh wave first overtone mode is known from simulations (Boué et al., 2016; Cruz-Atienza et al., 2016) and observed in sedimentary basins (Boué et al., 2016; Rivet et al., 2015; Savage et al., 2013). Boué et al. (2016) found that both fundamental and first higher modes have strong amplitudes in the period range 1–10 s, and while the first overtone has a higher phase velocity than the fundamental mode, they share a similar wave speed at the osculation point around 4.7 s. Boué et al. (2016) also found that wave propagation around the Hachioji Line (Figure 1) was marked by both a surface-wave reflection for the wavefield traveling within the basin and by a diffraction of the fundamental mode into the first overtone for wavefields traveling from outside to inside the basin. This latter effect is fully captured in our Green's functions: the wavefield outside of the basin is mainly a 2.5-km/s fundamental mode, while the waveforms recorded inside the basin (after a distance of 140 km in Figure 2) travel at a much lower speed of about 300 m/s for the fundamental mode and 500 m/s for the first higher mode (Boué et al., 2016; Denolle, Miyake, et al., 2014).

To discern the fundamental from the first higher mode in the waveforms, we investigate the polarization of the Rayleigh wave on the vertical-radial plane. Boué et al. (2016) found that, given a local 1-D velocity profile (Koketsu et al., 2009), the fundamental mode has a retrograde particle motion, while the first overtone has a prograde particle motion within the frequency band of interest. Ma et al. (2016) drew similar conclusions from observations in the Los Angeles Basin. The polarization of Rayleigh waves is expected to be elliptical

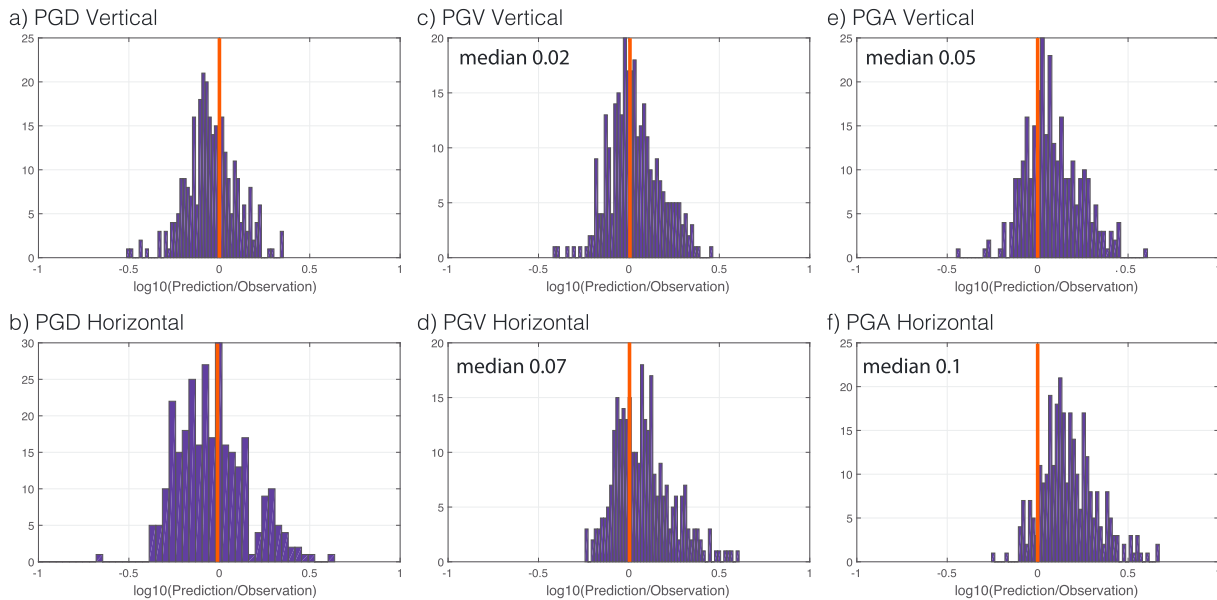


**Figure 4.** Histograms of the ratio of predicted and observed peak ground motion (horizontal and vertical) for the Nagano earthquake. Redline highlights an accurate prediction. (a) and (b) show the PGD fit, (c) and (d) show the PGV fits, and (e) and (f) show the PGA fits. PGA = peak ground acceleration; PGD = peak ground displacement; PGV = peak ground velocity.

in the radial-vertical receiver plane. Ma et al. (2016) and Gribler et al. (2016) proposed a filter to isolate the fundamental and the first higher modes based on their polarization.

The cumulative unwrapped phase  $\phi(t)$  between the RR and RZ (radial impulse force at the source and radial-vertical components at the receiver) and that between the ZR and ZZ (vertical impulse force at the source and radial-vertical components at the receiver) has increasing and decreasing trends with time. With our convention of vertical component positive downward, the positive slopes correspond to retrograde and the negative slopes to prograde particle motions. By taking the polarization function as the sign of the time derivative of  $\phi(t)$ , we can average the polarization functions within distance bins and sort the function with increasing distance. A coherent signal emerges from the polarization functions (Figure 3). At short distances from the source FM1H, that is, for paths completely outside the basin, the retrograde particle motion reflects the dominance of the fundamental mode. At greater distances for paths that cross the basin edge (Hachioji Line), the particle motion reflects the presence of the faster first overtone followed by a slower fundamental mode. Note that outside of the basin the shaking duration is much shorter compared to inside the basin (Figures 2 and 3).

Figure 2 shows that there are clear seismic signals in the cross terms ZT-TZ-RT-TR. Those components of the surface-wave Green tensor should be null in a laterally homogeneous media (e.g., Aki & Richards, 2002); however, in the real Earth there are multiple mechanisms to leak seismic energy into those components. First, because of the concave geometry of the basin, it is possible that incoming Rayleigh waves excite Love waves at the boundary and vice versa. In a body-wave formulation, this entails a coupling of  $P-S_V$  and  $S_H$ . Second, the assumption of straight ray paths between source and receivers is unlikely to be satisfied: with velocity changes as high as a factor of 3 between outside and inside the basin (Koketsu et al., 2009), the rays should experience strong lateral bending such that the R and T components would deviate from expectations based on that assumption. We have explored the possibility of employing the Optimal Rotation Algorithm (Roux, 2009) previously used for measures of anisotropy in near-field Green's function in Parkfield, California. The goal would be to solve for a different outgoing incidence angle and the incidence angle, instead of a single azimuth angle, by minimizing the amplitudes of the cross terms. One metric of success in decoupling the Rayleigh from Love waves is to compare the polarization functions as in Figure 3 before and after rotation. While we found spatial correlation in the best fitting angles, the polarization functions did not increase in strength (i.e., loss of coherence) as would be expected if ray bending were the predominant source of apparent coupling. For this reason we decided not to pursue optimal rotation and instead to neglect the cross terms.

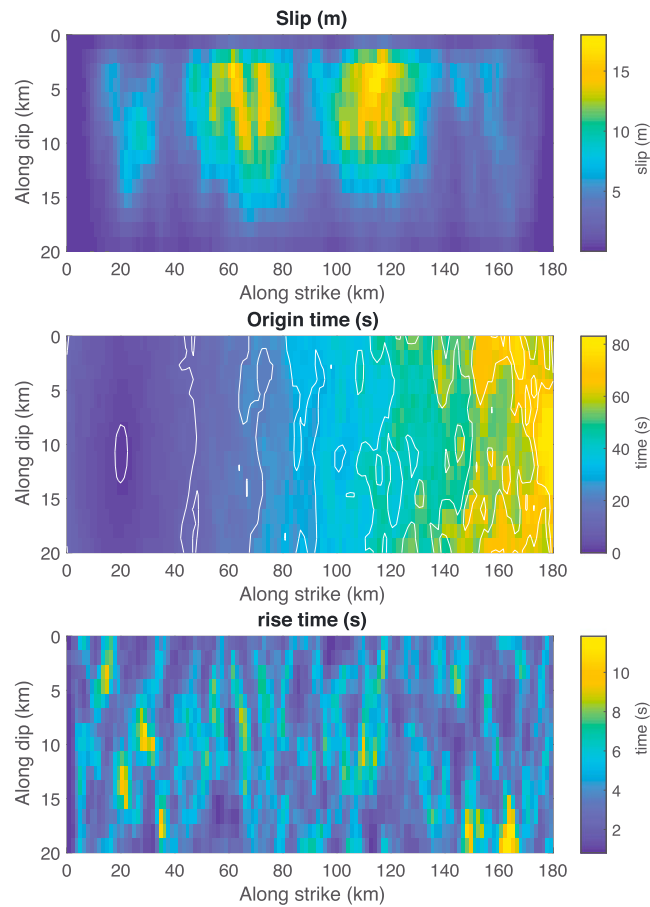


**Figure 5.** Representative example of a source model showing slip, rupture time, and rise time.

### 3. Setting Up Sources on the ISTL

The surface expression of the main fault in the ISTL has variable geometry (see Figure 1; Nakata & Imaizumi, 2002). The Japan Seismic Hazard Information Station also indicates that the ISTL has variable dip angles along the segments that could rupture together (Okumura, 2001). While fault geometry can be represented in kinematic source representation through pseudo-dynamic models (Mai et al., 2017), we preserve a simple planar geometry of the fault with the fault trace shown in Figure 1 and with a dip angle of  $70^\circ$ .

#### 3.1. Hi-Net Sources

Similar to Denolle, Dunham, et al. (2014), we choose for each pixel (point source) a phase-shifted Green's function from the closest Hi-net station. The VEA requires knowledge of the surface-wave dispersion for each virtual source, which we solve using the Generalized Eigenproblem Spectral Collocation (Denolle et al., 2012). We assume that the elastic medium close to the source is laterally homogeneous, and we select the velocity profile at each Hi-net station from Japan Integrated Velocity Structure Model (JIVSM; Koketsu et al., 2009). The velocity profiles close to the stations extracted from the JIVSM exemplify the case of a homogeneous elastic half space since the velocity variations are trapped in the near surface, which are less sensitive in the 1- to 10-s period band. To validate this, the cross-correlation functions from the virtual sources to MeSO-net stations on bedrock sites (see Figures 2, 3, S1, and S3) exhibit simple wave packet with little dispersion of the fundamental mode. This suggests that despite the narrow and thick sediments Matsumoto and Niigata tectonic valleys that may not be well represented in the JIVSM model, the surface-wave waveforms are as simple as those in a homogeneous halfspace in the 1- to 10-s period band. At those frequencies, the surface waves are dominated by fundamental modes and their dispersion is weak (Boué et al., 2016). This supports our results in Figures 2 and 3 that show only the fundamental mode and narrow waveforms for receivers outside the basin.

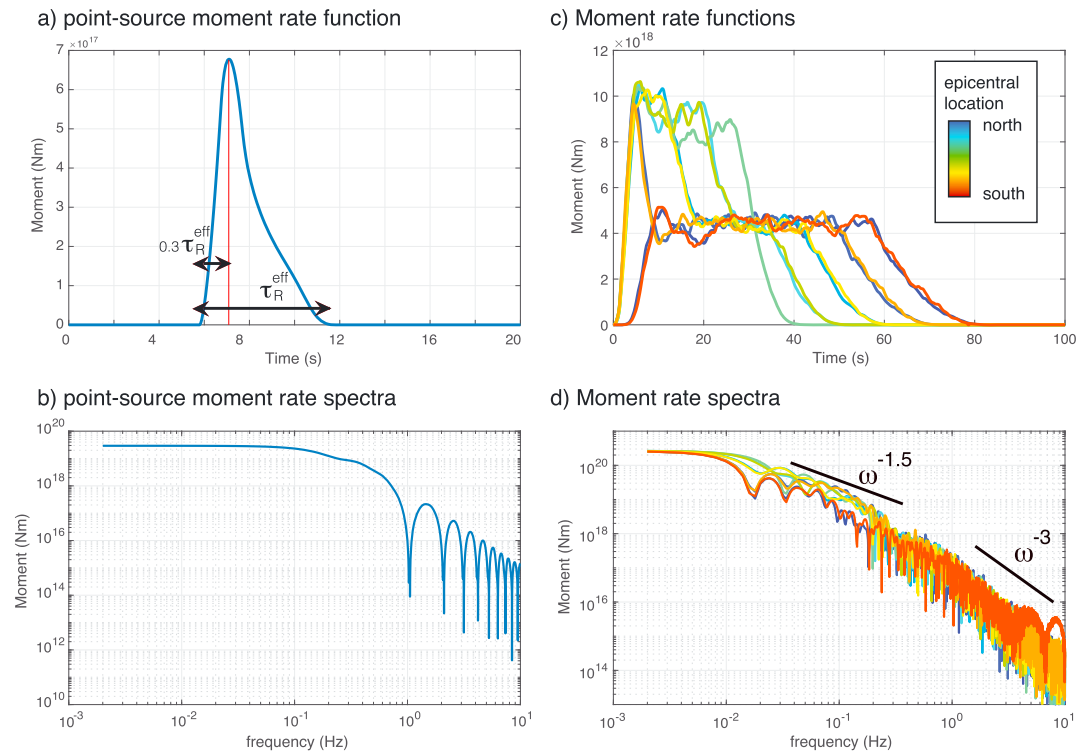


**Figure 6.** Example of the moment rate functions used in this study. (a) and (b) show example of a single slip function chosen at an individual point on the fault in the time and frequency domains. (c) and (d) show the whole-event moment rate functions, arithmetically averaged and colored for each epicentral location in the time and frequency domains: Blue is the unilateral rupture from the northern end, and red is the unilateral rupture from the southern end. Asymptotes at intermediate and high frequencies are shown in black.

Given that the first higher mode results from a secondary excitation due to the dynamic stresses of a fundamental mode at the basin edge, we only perform the VEA using the fundamental mode excitation and perform the same correction for the full waveform. Note that if higher modes were excited at the source, the VEA could be applied to each mode separately, provided that we separate or decouple the modes using, for instance, the polarization filter.

### 3.2. Calibration With the 2014 Northern Nagano Earthquake

The cross-correlation functions obtained from equation (1) in the Kanto region provide reliable relative amplitudes. First, this is confirmed by Viens et al. (2017). Second, the travel paths share a narrow azimuthal aperture between virtual sources and receivers and are mostly east-west, which is the dominant ambient wavefield propagation direction outside the basin. Finally, the amplitudes are dominated by the effects of the sedimentary basin (amplifications and reverberations; Figure S6). These dominant effects strongly mitigate the amplitude biases due to inherent variability in correlation function sensitivity to noise sources as discussed in Stehly and Boué (2017) for a line of receivers.

Given that only reliable relative information on the amplitudes is retrieved, a calibration to absolute amplitude levels of the Green's function, the factor  $C$  in equation (1), is necessary. Denolle, Dunham, et al. (2014) used a local moderate-sized earthquake that was close to a seismic station to establish a calibration factor. Because the noise-source distribution in southern California had strong azimuthal variations in amplitudes, Denolle, Dunham, et al. (2014) constructed an azimuth-dependent calibration factor. In our study, any azimuthal variations due to nonuniform noise sources are masked by the basin amplification and reverberation such that we assume that the calibration factor does not depend on azimuth.

We use the 22 November 2014 M6.2 Northern Nagano earthquake (National Research Institute for Earth Science and Disaster [NIED] centroid location  $36.689^{\circ}\text{N}$ ;  $137.890^{\circ}\text{E}$ ), which is located 3.9 km from the Hi-net station HBAH, to establish the calibration factor. The earthquake ruptured to the surface, but the highest moment release was at 5-km depth (NIED, Panayotopoulos et al., 2016). We choose the NIED tensor solution

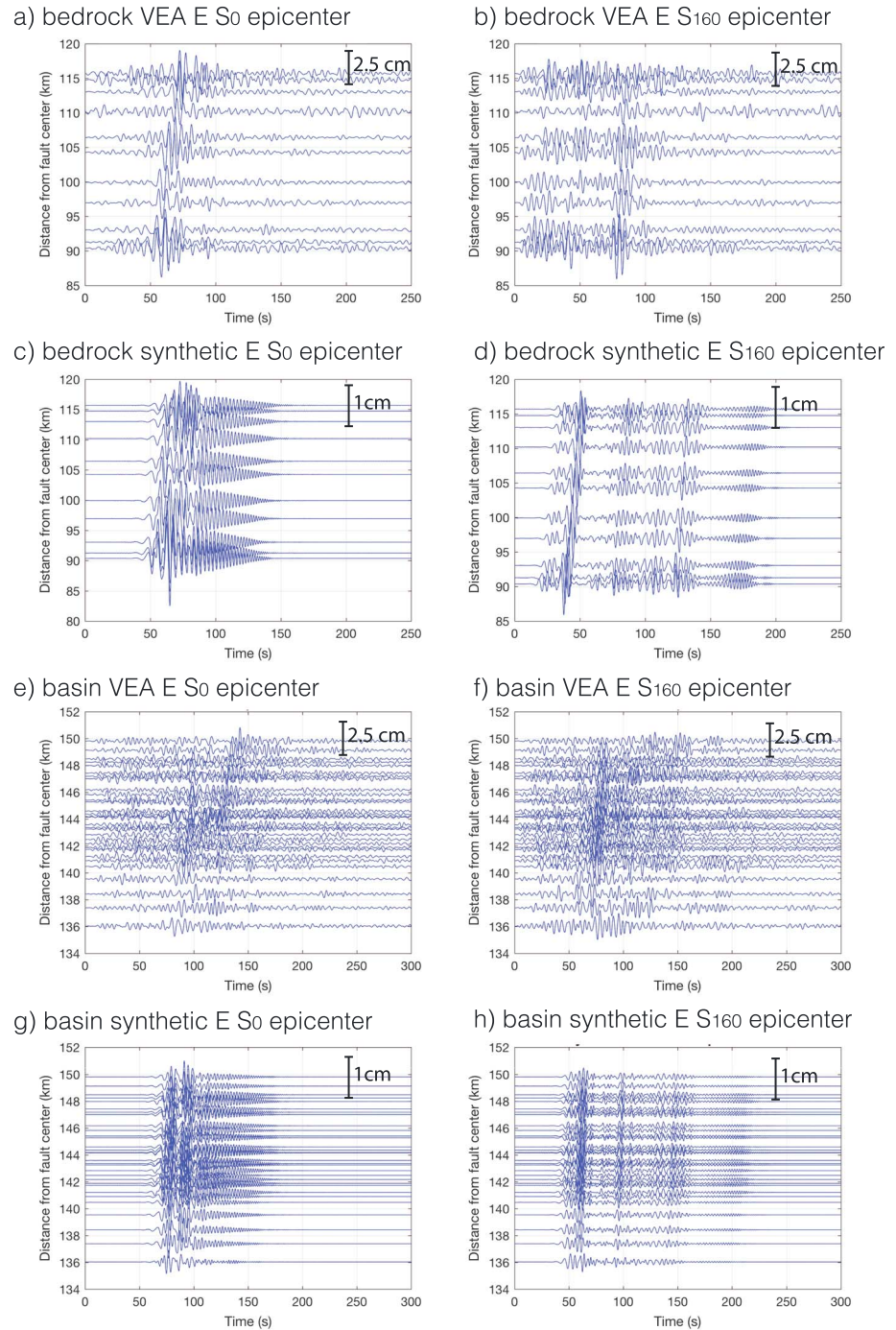


**Figure 7.** Displacement waveforms of the east component (approximately Rayleigh waves) for two scenario ruptures ([a, c, e, and g]  $S_0$  and [b, d, f, and h]  $S_{160}$ ; Figure 1 for selected bedrock sites, where the basement depth is shallower than 500 m). VEA = virtual earthquake approach.

with a rake of  $59^\circ$ , a dip of  $80^\circ$ , and a strike of  $358^\circ$ . We assume the moment rate spectrum of this event follows an  $\omega^{-2}$  model,

$$\hat{M}_0(\omega) = \frac{M_0}{1 + (\omega/\omega_c)^2}, \quad (2)$$

with a corner frequency  $f_c = \omega_c/2\pi = 1/T_d$  chosen to match the half duration  $T_d = 3.2$  s as assumed in the Global Centroid Moment Tensor solution (Ekström et al., 2012).

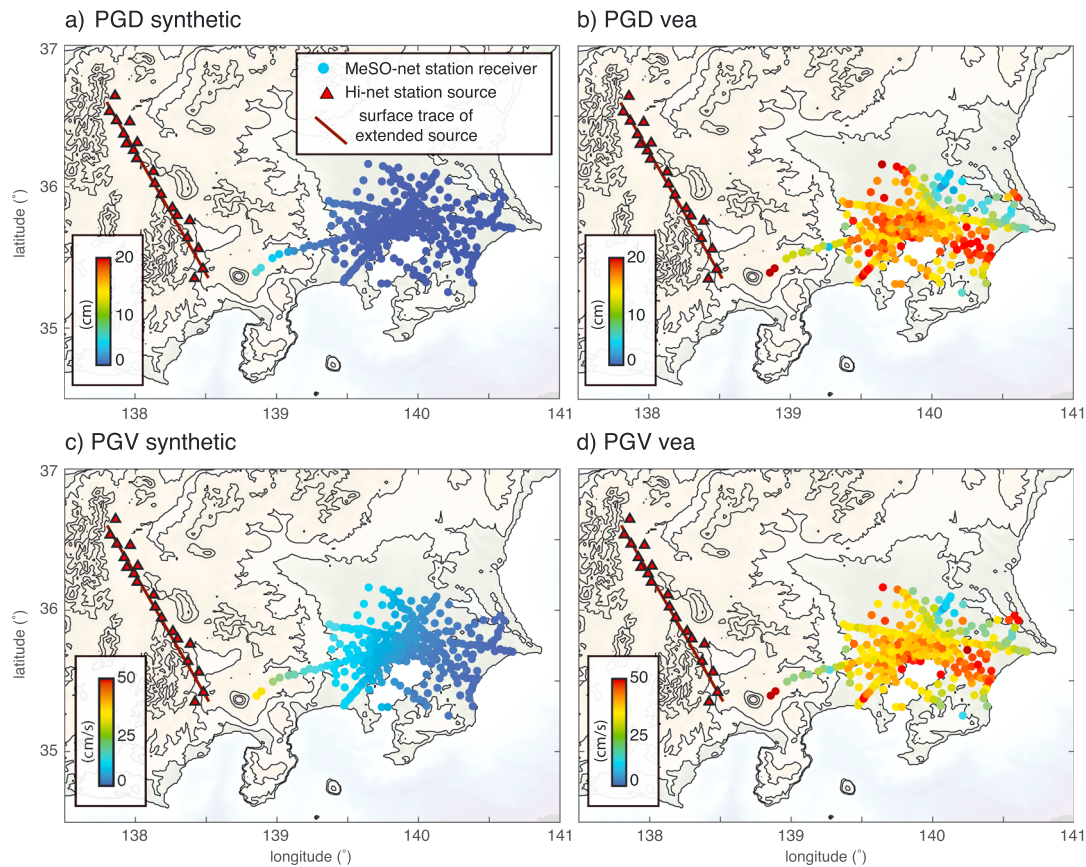


**Figure 8.** H/V ratios from (a) displacement waveforms for all sites and over all proposed scenario and (b) their median at each site. Topography is shown in colorscale and extracted from [topex.ucsd.edu](http://topex.ucsd.edu) (Smith & Sandwell, 1997). H/V = horizontal to vertical.

HBAH is located at the northern end of our virtual array, and the signal-to-noise ratio of the cross correlation is the lowest among our source stations (see the Green tensor in Figure S1). Nonetheless, we use this station to perform the VEA and calculate a calibration factor. The factors are calculated with the median (or mean in log) of the peak ground displacement (PGD) for the vertical, radial, and transverse components. Despite the high noise levels in the cross correlations due to the incomplete stacking of incoherent noise sources, the waveform fit at most sites is reasonable after calibration (Figures S7–S12 and S14–S16).

Common metrics in ground motion predictions are the PGD, peak ground velocity (PGV), and peak ground acceleration (PGA). These measures are taken in the horizontal plane, by finding the azimuth (or angle) at which the peak amplitudes are reached. Section 4.3 introduces an interpretation of that angle. After calibration, we compute the predicted and observed PGD, PGV, and PGA.

Figure 4 shows that the  $\log_{10}$  of their ratios provides a reasonable fit to the PGMs; the residuals appear to follow a lognormal distribution. The fit to the vertical PGM is better than that of the horizontal components. This is likely due to the greater signal-to-noise ratio for the vertical components. The signal-to-noise ratio is particularly low for the Love waves on the TT components (see Figure 2). The fit to the horizontal PGV and PGA is poorer (Figures 4d and 4f) and the VEA systematically overpredicts the shaking levels: the mean of the natural log of PGV is 0.17 and that of PGA is 0.22, yielding an overprediction of 19% and 24% for PGV and PGA, respectively. Because the differences between displacement, velocity, and acceleration reside in the frequency content, Figure S13 shows a comparison between the individual (and averaged) acceleration spectra from observed and predicted, after calibration to true displacement amplitude. The horizontal spectra are well calibrated to the peak amplitude spectrum within the frequency band, but the data have stronger low-frequency content than the predictions. It is interesting to note that the maximum spectral amplitude of the accelerations is at long periods, around 6 s, which corresponds well to the reported long-period resonance of the basin (Denolle, Miyake, et al., 2014; Miyake & Koketsu, 2005). The decay at higher frequencies

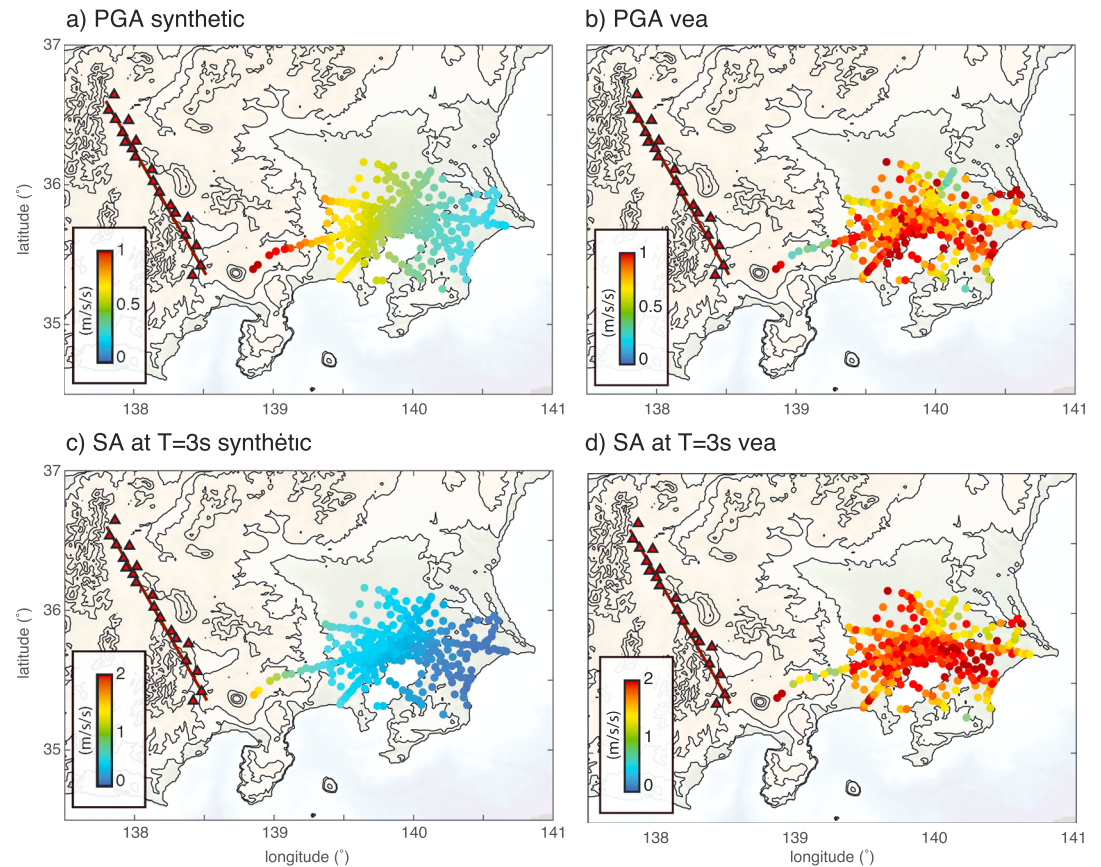


**Figure 9.** Median peak ground motion (displacement, velocity) for virtual earthquake and synthetics: Peak horizontal ground displacement (PGD) for synthetics (a) and VEA (b) in centimeters and peak ground velocity PGV for synthetics (c) and VEA (d) in cm/s. Topography is shown in colorscale and extracted from [topex.ucsd.edu](http://topex.ucsd.edu) (Smith & Sandwell, 1997). Hi-net = High-Sensitivity Seismograph network; MeSO-net = Metropolitan Seismic Observation network; PGV = peak ground velocity; VEA = virtual earthquake approach.

likely reflect seismic attenuation between Nagano and sites in the Kanto Basin. The predicted vertical spectra within the frequency band are relatively similar to the observed spectra, while the horizontal predictions seem to agree better at long periods (5–10 s). It is notable that the VEA waveforms are band limited due to high noise levels at frequencies greater than 0.8 Hz (or periods shorter than 1.25 s) and at frequencies lower than 0.1 Hz (or periods greater than 10 s; Figure S13). The high-frequency cutoff may be explained by insufficient coherent signal at those high frequencies due to attenuation, while the long-period cutoff is likely due to the sensitivity of the Hi-net short-period instruments.

The distributions of the residuals in Figure 4 are interesting in several respects. First, the standard deviation of the natural log of PGV and PGA are 0.33 and 0.34, respectively, values that are lower than the intraevent residuals reported from ground motion predictions using ground motion prediction equations (GMPEs; Baltay et al., 2017; Campbell & Bozorgnia, 2014; Villani & Abrahamson, 2015). This suggests that virtual earthquakes have the potential to improve on GMPEs. Second, the distributions allow us to establish the component of the epistemic uncertainty in the VEA that is due to the calibration. We take the calibration factors, separately for the horizontal components and for the vertical components, reduced by 1 standard deviation and those augmented by 1 standard deviation of the PGD log ratios to construct a low-level and a high-level prediction. We report that the resulting epistemic uncertainties are within a factor of 2, that is, either overpredicting or underpredicting by a factor of 2. Third, the level of residuals between horizontal and vertical components are similar.

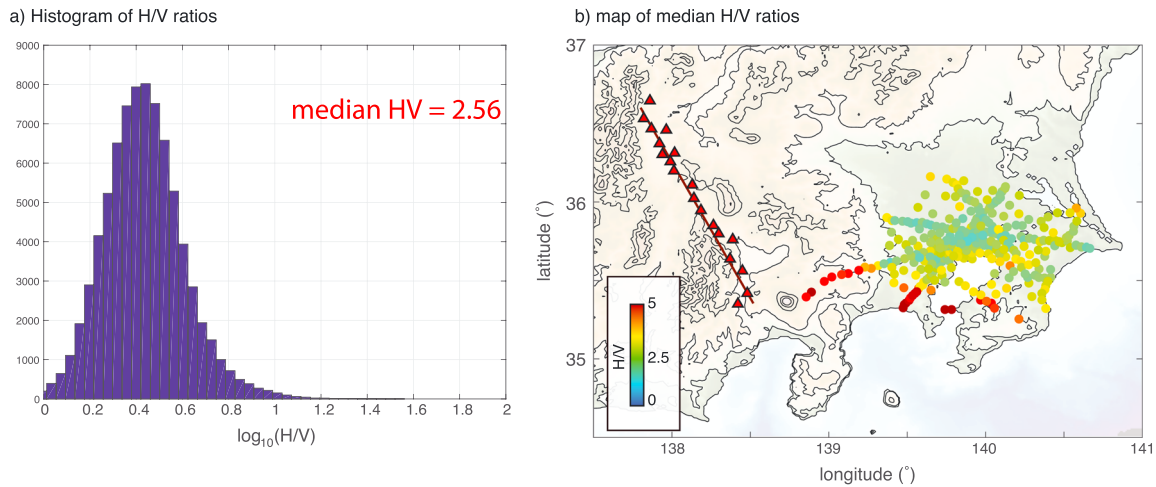


**Figure 10.** Median peak ground motion acceleration and SA for virtual earthquake and synthetics. (a) Synthetic PGA (in  $\text{cm/s}^2$ ), (b) VEA PGA (in  $\text{cm/s}^2$ ), (c) synthetic SA at  $T = 3$  s (in  $\text{cm/s}^2$ ), and (d) from VEA (in  $\text{cm/s}^2$ ). Topography is shown in colorscale and extracted from [topex.ucsd.edu](http://topex.ucsd.edu) (Smith & Sandwell, 1997). PGA = peak ground acceleration; SA = spectral acceleration; VEA = virtual earthquake approach.

Finally, we also show that the predicted and observed horizontal-to-vertical (H/V) ratios are similar (Figure S17), with a median value of 3 for the earthquake and 3.13 for the VEA ground motions. The misfit is more pronounced for sites that are located outside the basin (for stations located in the azimuthal  $135^\circ - 145^\circ$  from HBAH).

### 3.3. Kinematic Source Generator

The source is a planar fault of dimension  $160 \times 20$  km with a strike of  $150^\circ$  and a dip of  $70^\circ$ . We simulate a M7.6 with an averaged slip of about 5 m. We choose a kinematic source generator (Crempien & Archuleta, 2015; Mai & Beroza, 2002; Schmedes et al., 2013) that is statistical and that respects the correlations between source parameters found in dynamic simulations (Schmedes et al., 2010). The source generator prescribes a distribution of slip (amplitudes are drawn from a truncated Cauchy distribution), rise time (duration of active slip), and rupture velocity that follows a  $k^{-2}$ ,  $k^{-1.75}$ ,  $k^{-0.83}$  spatial distribution ( $k$  being the spatial wave number). We impose a correlation length of 20 km for the slip distribution. We perform 30 realizations of slip, rise time, and rupture velocity, and select nine epicentral locations evenly spaced by 20 km. The rupture time is found by solving the wave equation (Crempien & Archuleta, 2015; Frankel, 2009; Schmedes et al., 2013).

We compute 270 realizations of kinematic sources. The hypocenter is fixed at 9.4-km depth (10 km down dip from the surface). The rupture velocity  $V_r$  averages approximately  $0.88\beta$ , where we choose the shear wave speed of  $\beta = 3.2$  km/s,  $V_r = 2.88$  km/s. In these realizations, we do not include perturbations in the moment tensor and simulate an oblique thrust mechanism with a rake of  $45^\circ$  to represent a combination of thrust mechanism to the north (Sagiya et al., 2004) and left-lateral mechanism to the south (Kondo et al., 2006).

The choice of epicentral locations allows us to evaluate the effects of source directivity onto the predictions of ground motion: An epicenter to the north will simulate a unilateral southward rupture or toward Tokyo; an epicenter to the south will simulate a unilateral rupture to the north, away from Tokyo; and an epicenter in the middle of the fault illustrates scenarios of bilateral ruptures. Figure 5 shows an example of such a scenario source with the distribution of moment for each point source, the rupture time for an epicenter located at 20 km of the northern edge, and the rise time.

At each pixel  $i$ , the moment rate function is

$$\dot{M}_0^i(t) = M_0^i \dot{s}^i(t), \quad (3)$$

where  $M_0^i$  is the moment at the point source (pixel)  $i$  and  $\dot{s}^i(t)$  is the slip rate function normalized such that over the source duration  $\tau^i$ ,  $\int_0^{\tau^i} \dot{s}^i(t) dt = 1$ . To respect a parametrization of the slip rate function that is typically found in dynamic rupture simulations (Mai et al., 2017; Schmedes et al., 2013; Tinti et al., 2005), the slip rate

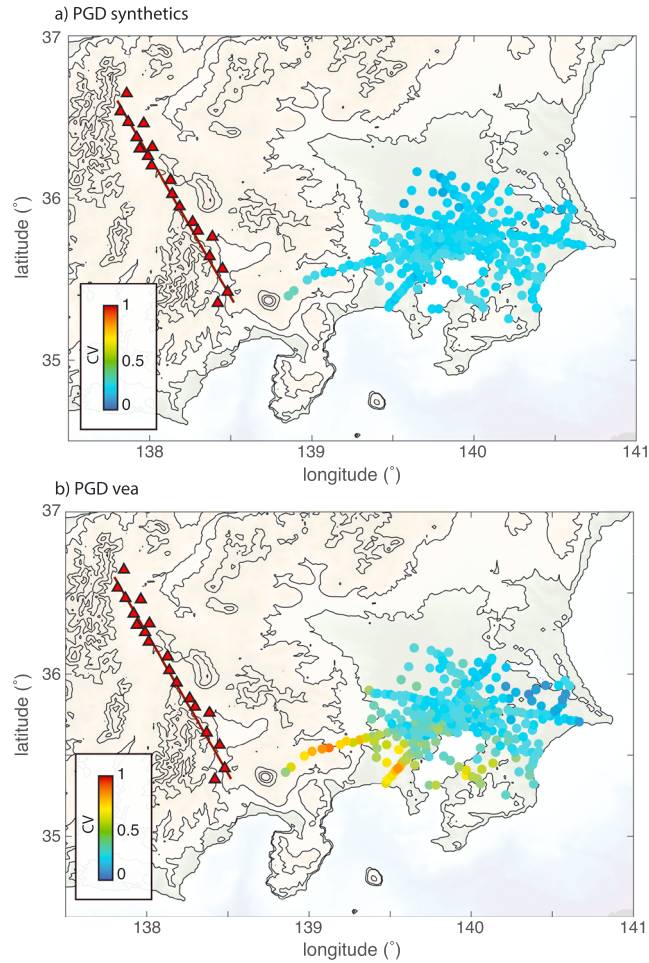


**Figure 11.** Coefficient of variation coefficient of variation of PGD for (a) synthetics and (b) VEA. Topography is shown in colorscale and extracted from topex.ucsd.edu (Smith & Sandwell, 1997). PGD = peak ground displacement; VEA = virtual earthquake approach.

function is a regularized Yoffe function (Tinti et al., 2005), that is, a convolution of a truncated Yoffe function  $Y(t)$  with a triangle function  $W(t)$ :

$$s_0^i(t) = A \int_0^T Y(t, \tau_r^i, t_0^i) W(t - \tau, \tau_s^i) d\tau, \quad (4)$$

where  $\tau_r^i$  represents the rise time,  $t_0^i$  represent the onset time of the subfault indexed  $i$ , and the factor  $A$  is the slip normalization factor. The truncated Yoffe function is

$$Y(t, \tau_r, t_0) = \frac{2}{\pi \tau_r} H(t - t_0) H(\tau_r - t - t_0) \sqrt{\frac{\tau_r - (t - t_0)}{t - t_0}}, \quad (5)$$

where  $H(t)$  is the Heaviside function.  $\tau_r$  is the local rise time,  $\tau_s^i$  is the width of the triangle function such that the effective rise time  $\tau_r^{eff}$  is larger than  $\tau_r$ ,  $\tau_r^{eff} = \tau_r + 2\tau_s$ . The triangle function is

$$W(t) = \frac{1}{\tau_s^2} [H(t)H(\tau_s - t) + (2\tau_s - t)H(t - \tau_s)H(2\tau_s - t)]. \quad (6)$$

We draw  $\tau_r^{eff}$  from the distributions to be consistent with the source parameter correlations (Crempien & Archuleta, 2015). We choose a time to peak velocity fixed at  $0.3\tau_r^{eff}$  and using the scaling found in Tinti et al. (2005), we select the triangle function half width as  $\tau_s = 0.3\tau_r^{eff}/1.27$ . In our realizations, the average rise time  $\tau_r^{eff}$  is around 4.5 s.

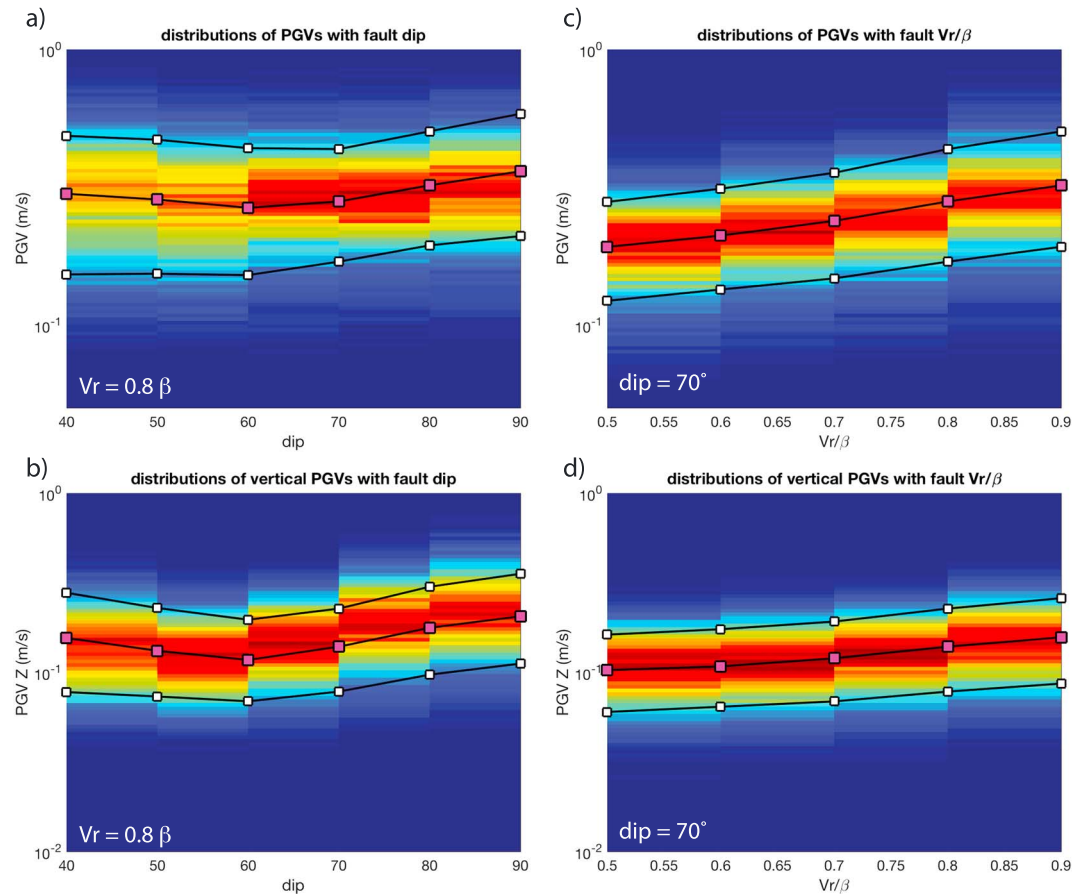


**Figure 12.** Sensitivity of the velocities (PGV) with various fault dip and rupture velocity for planar faults with median and the 10% and 90% percentiles as a measure for average and spread of the distributions of peak ground motions. PGV = peak ground velocity.

Figure 6 shows an example of such a function after summation of all point sources and averaged over the 30 scenario sources of a given epicenter. The pulse shape is characteristic of self-healing pulses (Heaton, 1990; Nielsen & Madariaga, 2003) with a local rise time much shorter than the overall source duration. The presence of an intermediate slope in the amplitude spectrum has recently been observed in moderate-to-large crustal earthquakes (Archuleta & Ji, 2016; Boatwright & Choy, 1989, 1992) and for global thrust events (Denolle & Shearer, 2016).

### 3.4. Synthetic Waveforms in a Laterally Homogeneous Medium

We use the surface-wave eigenfunctions and wave numbers to compute the far-field surface waves (Aki & Richards, 2002; Denolle et al., 2012), the representation theorem to sum the sources from the kinematic models, and we construct the seismogram at all MeSO-net receivers. We attribute a local velocity profile to each virtual source, extracted from the community velocity model JIVSM (Koketsu et al., 2009). At each site, we solve for the surface-wave eigenfunctions (Denolle et al., 2012) assuming that the medium is laterally homogeneous and construct the five nonzero components of the synthetic Green tensor. The velocity model is taken outside of the sedimentary basin to highlight the contrast between the VEA prediction and the assumption of a 1-D structure (laterally homogeneous). In the frequency band of our study, the variations in velocity models between the Hi-net station locations do not generate noteworthy differences in surface-wave eigenfunctions. Finally, the medium is described as purely elastic, and we do not account for attenuation in constructing the synthetic waveforms. Additionally, we have assumed that attenuation is incorporated in the ambient seismic field, and thus, we shall expect that synthetics would overpredict the amplitudes. Besides attenuation, the main difference resides in the contrast between 3-D velocity structure of the basin and the laterally homogeneous (referred to as 1-D) used in the synthetics.

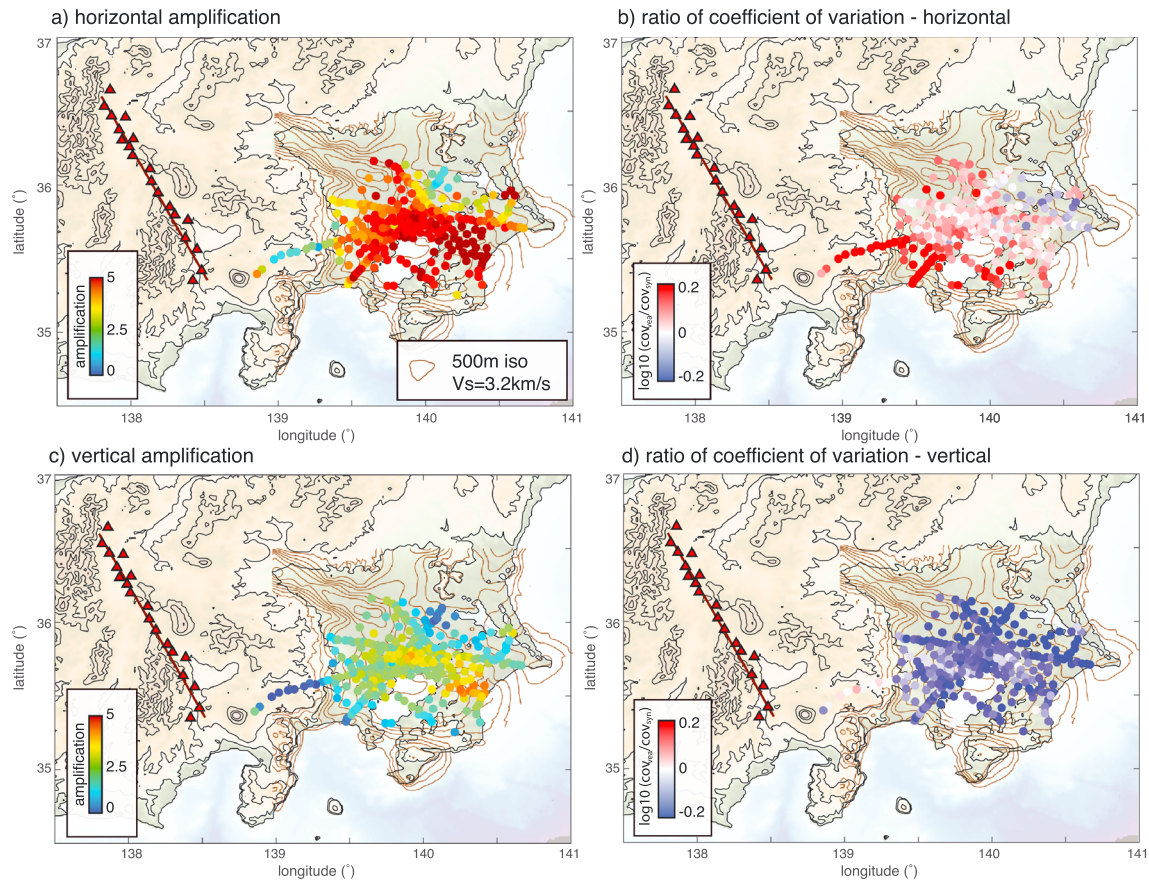


**Figure 13.** Comparison of the virtual earthquake approach displacements relative to 1-D synthetics for (a) peak ground displacement and (b) ratio of the coefficient of variation for horizontal components; (c) and (d) are same as in (a) and (b) but for vertical ground motions. Topography is shown in colorscale and extracted from topex.ucsd.edu (Smith & Sandwell, 1997) and basin contours are the iso  $V_S = 3.2$ -km/s contours (Koketsu et al., 2009).

### 3.5. Virtual Earthquake Waveforms

We perform the similar technique as in Denolle, Dunham, et al. (2014). The kinematic sources are discretized over grid points whereby each grid point is a small double-couple source with a specific moment rate function. For each grid point, we perform the similar approach as for the Nagano earthquake (source depth and mechanism correction, i.e., Denolle et al., 2013). Each point source correction provides a three-component seismograms rotated into individual radial-transverse-vertical framework. We rotate these seismograms into the regional north-east-vertical coordinate system and stack these over all point sources of the extended source using the principle of superposition. The final set of waveform is a three-component displacement seismograms (north, east, and vertical) at each receiver and for each source. To analyze the results, we differentiate in time the waveforms to evaluate also ground motion strength in velocity and accelerations.

## 4. Results and Discussion

### 4.1. Scenario Earthquakes

We construct a total of 270 scenario earthquakes for ground motion prediction using the VEA approach. The resulting database contains almost 240,000 waveforms. We show examples of waveforms in Figure 7, where we compare selected basin and bedrock sites.

Additional examples of such waveforms are shown in Figures S19–S21. However, rather than comparing individual waveforms, we use metrics of ground motion common to earthquake engineers: the PGMs taken in time domain (PGD: displacement, PGV: velocity, and PGA: acceleration) and the spectral acceleration (SA) for a single degree of freedom oscillator with a damping of 5%. SA is a ground motion metric that is often used in GMPEs and routinely estimated for earthquakes by the United States Geological Survey and they allow for a direct comparison with outputs from GMPEs. While buildings are more sensitive to shear and thus

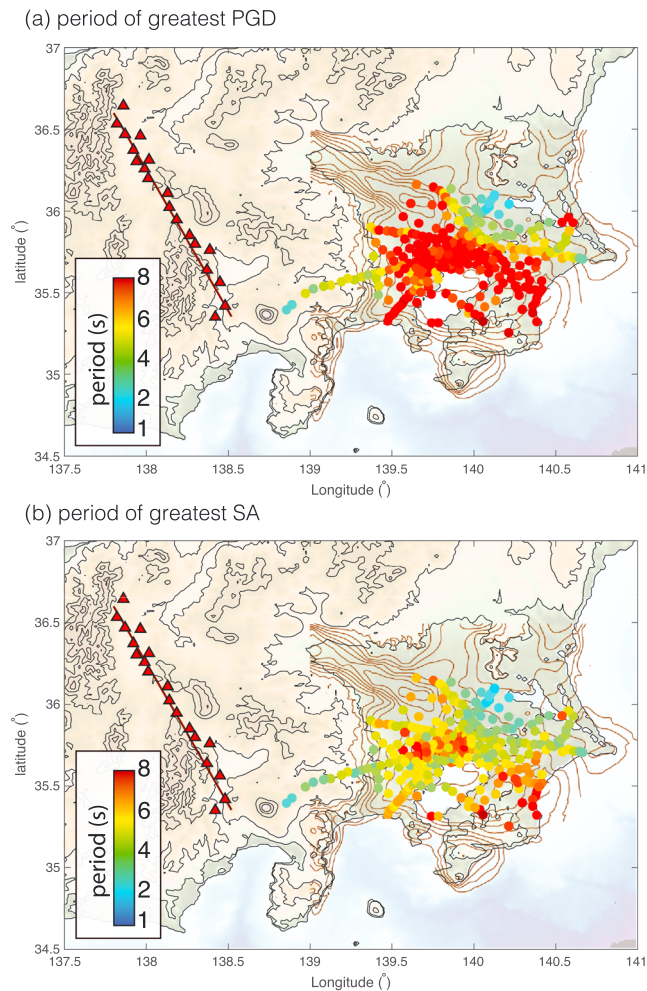


**Figure 14.** Median seismic periods of greatest shaking for (a) horizontal displacements PGD and (b) spectral accelerations (SAs) estimated over all 270 scenario sources. Topography is shown in colorscale and extracted from [topex.ucsd.edu](http://topex.ucsd.edu) (Smith & Sandwell, 1997), and basin contours are the iso  $V_s = 3.2$ -km/s contours (Koketsu et al., 2009). PGD = peak ground displacement.

to horizontal ground motions, we also discuss the vertical ground motions. The PGM values are found by rotating the horizontal seismograms to the angle at which PGM is reached.

For each site, we calculate the median of the PGMs for the entire set of 270 scenario earthquakes since they are approximately lognormally distributed. We also take the interquartile range (iqr, 25%–75%) instead of standard deviation as a measure of variability. The absolute difference in levels between the synthetics and the VEA ground motions may be explained by the simplified model set up for the synthetic case. The medium is assumed purely elastic, for example, without attenuation, and the velocity profile chosen at each source is that of a bedrock upper crust, with no excitation of higher modes in the frequency band of this study.

The PGM levels of the VEA scenario earthquakes are predicted to be quite large: the median PGD is 20 cm (the median + 1 iqr is 30 cm), the median PGV is 32 cm/s (the median + 1 iqr is 46 cm/s), and the median PGA is  $74 \text{ cm/s}^2$  ( $\sim 0.7\% g$ , the median + 1 iqr is  $1 \text{ m/s}^2$ ,  $\sim 10\% g$ ). These values are similar to those found by Denolle, Dunham, et al. (2014) for a M7.2 San Andreas event recorded in Los Angeles. The median level is controlled by the calibration to the Nagano earthquake and thus may be uncertain by a factor of 2. The peak period of resonance of the basin is captured in the horizontal displacements (Figure 13a), which we find to be longer in the deepest parts of the basin (7–8 s) as against outside of the basin (2–4 s). We show in Figure 10d that SA at 3-s period peaks at high values (Figure S18),  $1.55 \text{ m/s}^2$  ( $\sim 15\% g$ , the median + 1 iqr is  $2.5 \text{ m/s}^2$ ,  $\sim 25\% g$ ). We find, however, that the peak period of the spectral acceleration varies throughout the basin (Figure 13b), with less spatial correlation than the period of resonance (Figure 13a). A comparison to previous ground motion

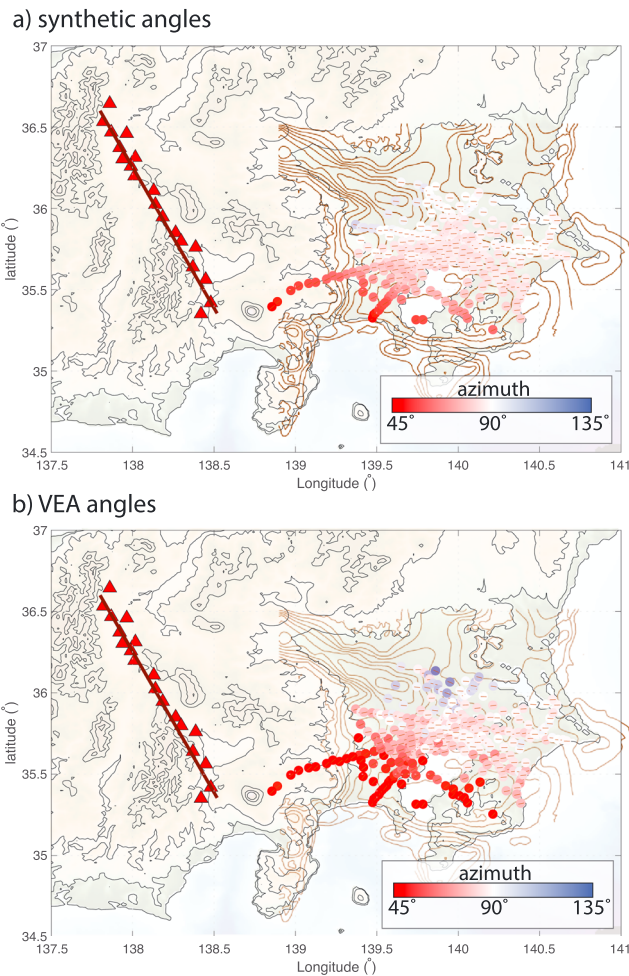


**Figure 15.** Median of the peak the azimuth of greatest horizontal displacement ground motion for (a) synthetic waveforms and (b) virtual earthquake approach (VEA) waveforms. Topography is shown in colorscale and extracted from [topex.ucsd.edu](http://topex.ucsd.edu) (Smith & Sandwell, 1997), and basin contours are the iso  $V_5 = 3.2$ -km/s contours (Koketsu et al., 2009).

measurements is needed to validate our results. Previous shaking intensities were observed for earthquakes in the vicinity of the ISTL. Furumura and Hayakawa (2007) reported and simulate ground motions for the 2004 M6.6 Niigata-ken Chuetsu earthquake with PGDs  $\sim 2$  cm, PGV  $\sim 2$  cm/s, and PGA  $\sim 20$  cm/s<sup>2</sup> (2% g). Using a simple omega-square source model with a corner frequency that varies such that the static stress drop on a circular crack equals 3 MPa, we can scale the expected PGMs and find that for a M7.6 local to Niigata would yield 28 times greater shaking displacement levels (i.e., PGD  $\sim 56$  cm), 10 times more PGVs,  $\sim 20$  cm/s, and 3 times more PGA,  $\sim 60$  cm/s<sup>2</sup> (6% g). Similarly, if we were to scale linearly the shaking levels observed during the Northern Nagano event, one might expect levels as high as PGD  $\sim 56$  cm, PGV  $\sim 16$  cm/s, PGA  $\sim 4$  cm/s<sup>2</sup> (4% g) for our scenario sources. Finally, Mikumo and Ando (1976) reported the PGD and PGV recorded in Nagoya during the M8 1891 Mino-Owari earthquake to be  $\sim 20$  cm and  $\sim 54$  cm/s, respectively, at distances of about 50 km.

The linear shaking levels are high, and nonlinear effects may reduce future ground motions from these scenario earthquakes. At these levels of PGVs, the Kanto area responds nonlinearly. Roten et al. (2014) and Roten et al. (2017) simulated long-period ground motions (periods greater than 2 s) for a large M7.8 scenario source on the San Andreas Fault (California) and showed a possible reduction of 70% in PGV, decreasing the expected  $\sim 2+$  m/s down to  $\sim 1$  m/s. A large proportion of that reduction occurred near the fault, but it also occurred during the wave propagation in sedimentary basins. Thus, we expect in a real earthquake that our linear predictions would be reduced by nonlinearity of the dynamic soil response.

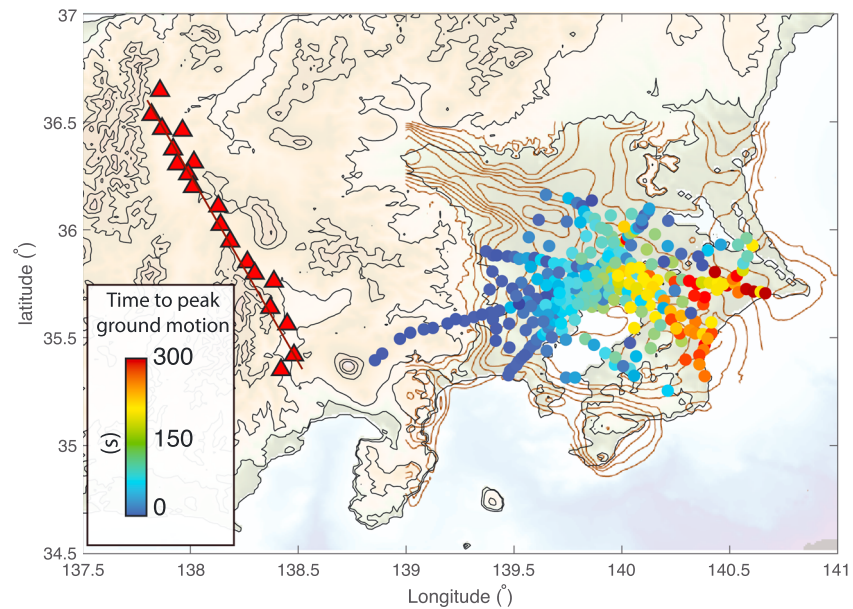


**Figure 16.** Time of the peak amplitude one scenario source  $S_{60}$ . Topography is shown in colorscale and extracted from [topex.ucsd.edu](http://topex.ucsd.edu) (Smith & Sandwell, 1997), and basin contours are the iso  $V_S = 3.2$ -km/s contours (Koketsu et al., 2009).

We estimate the H/V ratio as the PGD divided by the peak ground vertical displacement. The horizontal ground motion includes both Love and Rayleigh waves. For a laterally homogeneous medium, such as that used for the Hi-net stations, the median H/V ratio over all sites and all scenario sources is 2.09. The median H/V ratio observed during the Northern Nagano earthquake was 3, and the median H/V ratio predicted from the VEA is 2.56 (Figure 8). The H/V ratios are approximately lognormally distributed, with a distribution that exhibits a tail at high values (up to 80). The H/V ratio predicted by the VEA are higher than those predicted by a laterally homogeneous medium. Indeed, the horizontal component of the Rayleigh waves are known to carry strong amplitude in sedimentary layers (Savage et al., 2013). The high H/V values localize at the southwestern edge of Kanto Basin, where we expect the strongest PGDs (Figure 9b).

The spatial patterns of the synthetic PGMs display a simple geometrical spreading effect with shaking intensity decreasing with distance from the fault (Figures 9a and 9c, and 10a and 10c). Proximity to the fault is among the most important parameters in GMPEs (Douglas & Edwards, 2016). In contrast, the spatial pattern of the VEA PGMs clearly shows that the center of the Kanto Basin will experience stronger shaking at all frequencies (for PGD, PGV, and PGA). In this instance, proximity to the fault is not the main criterion for long-period strong ground motion, an expected result for basin amplification (Denolle, Dunham, et al., 2014; Denolle, Miyake, et al., 2014; Furumura & Hayakawa, 2007). Spatial variations of VEA shaking levels are also greater than the smoothly varying shaking levels predicted from synthetics.

The comparison between the VEA and the synthetics PGMs (Figures 9b and 9d, and 10b and 10d) demonstrates the relation between basin structure and ground shaking. The strongest ground motion locates near the deepest parts of the basin. In particular, the northern edge of the basin is where the strongest difference between the 3-D (VEA) and 1-D (synthetic) lie.

#### 4.2. Variability in Ground Motions Due To Uncertain Sources

We explore the variability in ground motion due to the uncertainties in potential future sources. We use a simple kinematic model on a planar fault and vary slip distribution, hypocentral location, fault dip, and average rupture velocity. At all sites, ground motions are lognormally distributed.

First, we explore over all 270 scenario sources the distributions of the PGMs. We modify the metric that is commonly used for variability with the ratio of the median over the interquartile range instead of the mean over the standard deviation of the PGDs. We keep the notation CV (coefficient of variation) despite this difference and use the horizontal displacements values. The variability in the synthetic PGMs is uniform throughout the basin (Figure 11a) with a median value of 0.31. In contrast, the variability predicted from VEA is greater

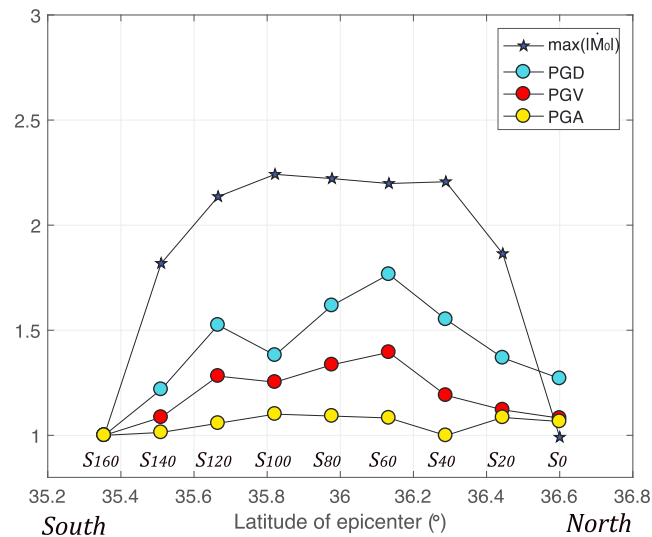


**Figure 17.** Peak of the moment rate function (blue stars), peak ground motions (PGD in cyan circles, PGV in red circles, and PGA in yellow circles) taken as the median + interquartile range), normalized to the southern epicenter (located at latitude 35.35, source  $S_{160}$ ) attributed to each epicenters. The y axis is the dimensionless ratio of peak amplitudes. The epicenters to the north ( $S_0$ – $S_{60}$ ) represent southward ruptures with directivity effects toward Tokyo. The epicenters to the south ( $S_{100}$ – $S_{160}$ ) represent northward ruptures, with directivity effects away from Tokyo. The epicenter in the middle ( $S_{80}$ ) represents bilateral ruptures. PGA = peak ground acceleration; PGD = peak ground displacement; PGV = peak ground velocity.

(median 0.34) and not uniform across Kanto Basin (Figure 11b). We discuss the likely role of the basin shape in the following section.

Because the ISTL may be segmented and has variable fault dip, we then investigated the variability in ground motions due to uncertainties in fault dip. Our reference model is a  $70^\circ$  dipping fault, and we carry out an experiment with fault dipping from  $40^\circ$  to  $90^\circ$ . Similar to our reference case, we construct 30 scenario sources and fix the epicentral distance to  $S_{80}$ . We explore the distributions of the ground motions at all ground motion metrics and show the PGV (horizontal and vertical) in Figures 12a and 12b. We find the lowest ground motions for a ISTL dipping at  $60^\circ$  and a greater ground motion for a pure vertical fault, in particular for the vertical ground motions (see Table S1). The ratio of the maximum to minimum median PGD for the vertical component is 1.74 and 1.23 for the horizontal components. Thus, one might expect an uncertainty in ground motions due to uncertain fault dip of 74% for the vertical ground motions and 23% for the horizontal ground motions.

We carry a similar experiment to establish the effects of rupture velocity on the PGMs. We construct a suite of scenario sources with a  $70^\circ$  fault, an epicenter located at  $S_{80}$ , and vary the rupture velocity from  $0.5\beta$  to  $0.9\beta$  (always sub-Rayleigh wave speed). The distributions of the ground motions are shown in Figures 12c and 12d and exhibit, as expected, an increasing trend from lower values for slow earthquakes to higher values for fast earthquakes. The fault dip affects more strongly the high frequencies (see Table S1). The ratio between the fast and slow ruptures 62% and 57% for the horizontal and vertical ground motion, respectively.

There are major limitations in using kinematic models on planar faults. First, the ISTL is likely composed of multiple segments and variable fault geometry, which we do not account for in this study. The effect of fault segmentation and geometrical complexity at various length scales onto the near-field ground motion are currently an active area of research (Aochi & Madariaga, 2003; Aochi & Ulrich, 2015; Lozos, 2016; Mai et al., 2017) and are computationally too expensive to produce populations of kinematic sources. While seismic moment may be largely released within a segment, the jumping from one segment to next may excite high-frequency ground motions (Adda-Bedia & Madariaga, 2008). A parametric description of such effects in kinematic models would improve the prediction of ground motions in complex fault systems. Such description may be modeled through dynamic modeling in future work.

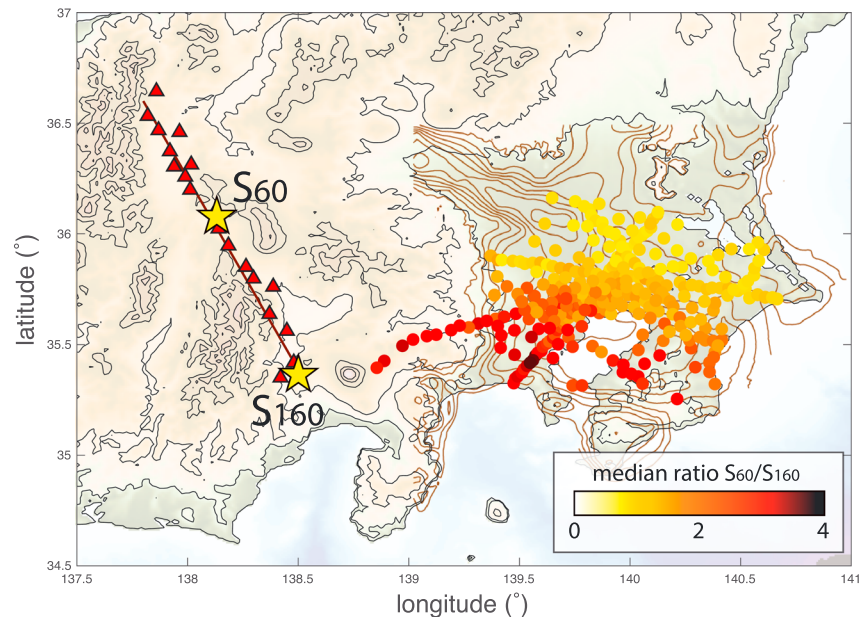


**Figure 18.** Median ratios of peak ground displacements from the scenario sources with the epicenter at the coupling point ( $S_{60}$ ) and at the southern edge of the fault model ( $S_{160}$ ). Topography is shown in colorscale and extracted from [topex.ucsd.edu](http://topex.ucsd.edu) (Smith & Sandwell, 1997), and basin contours are the iso  $V_S = 3.2$ -km/s contours (Koketsu et al., 2009).

#### 4.3. Effect of the Basin Shape on Ground Motions and Their Variability

To establish the role of the sedimentary basin and its shape to ground motions, we explore various characterizations of the wavefield (seismic amplification, ground motion variability, spectral content, wavefield polarization, and wavefield refraction) and relate their effects on ground motion variability.

First, we evaluate seismic amplification due to basin shape as the ratio of the median PGMs from VEA to those from the synthetics. The median seismic amplification of horizontal ground motion, as seen in Figure 13a shows shaking levels 5 times greater for the VEA than for the synthetic values. The amplification is lower than that previously discussed in Denolle, Miyake, et al. (2014) who proposed values as high as 15 times for sources on the ISTL. Here we find horizontal seismic amplification to be greater than the vertical amplification (Figure 13c), which may be explained by the VEA H/V ratios higher than the synthetic H/V ratios. Overlaying the contours of the basin basement depth (Figures 13a and 13c) shows a spatial correlation between seismic amplification and basin depth.

The difference in variability that can be attributed to 3-D wave propagation effects can be measured with the ratio of the VEA to synthetic displacement CV (Figures 13b and 13d). In general, the horizontal variability of the VEA predictions is greater than that of the synthetics in the southern part of the basin by about 60%. In contrast, it appears to decrease in the northern half of the area of interest. It reaches its lowest value (variability is lower for VEA than for synthetics) at the northern edge of the basin. The northern region encompasses Tokyo, Saitama, Chiba, and Narita, while the southern region encompasses Yokohama and the Boso Peninsula (see Figure 1). In contrast, the vertical variability of the VEA is reduced compared to that of the synthetic: The crustal structure appears to homogenize the wave propagation of vertical Rayleigh waves.

The sedimentary basin shape also tends to alter the frequency content of the strongest ground motion. Denolle, Miyake, et al. (2014) found that, when averaged over all sources, the ambient-field vertical displacement cross correlation were amplified mostly at 6 s. Our analysis also shows that the basin shape affects long periods (6–8 s) of the horizontal ground displacements (Figure 14a). The effect of the basin depth also affects the peak periods of spectral acceleration. In general, longer acceleration periods are expected in the central part of the basin (3–7 s), though the correlation with basin depth or sediment thickness is not as trivial (Figure 14b).

We explore the variation in the direction of greatest shaking. At each site and for each scenario source, we calculate the angle of polarization at which the PGD is the greatest. We take the median over all scenario sources

for the synthetic and VEA values and show them in Figure 15. In the synthetic examples (Figure 15a), the polarization of greatest shaking implies that Rayleigh waves dominate the horizontal components because the polarization in the laterally homogeneous medium is oriented along the source-receiver axis. The polarization of the VEA waveform instead indicates the strong wave refraction at the basin edges (Figure 15b). This is further supported by the distribution of the arrival times of the peak amplitudes (Figure 16), where the northern edge of the basin exhibit strong shaking relatively early compared to the central part of the basin. Indeed, strong refraction is expected to occur at the basin edges (Boué et al., 2016; Furumura & Hayakawa, 2007; Koketsu & Kikuchi, 2000). The most pronounced effect is seen in the seismic waveguide at the northern edge of the basin where the polarization is parallel to the basin edge. This indicates that the dominant phase in the waveform is either a Love wave or is a Rayleigh wave that drastically refracts along the basin edge. In contrast, the polarization at the southern edge is perpendicular to the basin edge, likely a signature of the strong radial component of the higher Rayleigh wave mode (Boué et al., 2016).

Wavefield refraction can be easily measured using the time of PGM. The JIVSM velocity model exhibit particularly strong contrast of seismic wave speeds across the basin walls, and one might expect seismic waves excited in the Niigata region to arrive faster on the northern and southern edges of the basin and later in the central part of the basin. Our results confirm this (Figure 16), with sites in the northern edge of the basin experiencing wave arriving at similar times than the southern edge.

Finally, the characteristics of the wavefield may explain the spatial variation in ground motion variability (Figure 11). The southwestern edge of the Kanto Basin experiences higher ground motion variability than the median synthetic CV, along with higher PGDs, while the northeastern part of the basin experiences lower ground motion variability. Seismic waves have to travel through the seismic waveguide before reaching those MeSO-net sites, and we suggest that a reduced ground motion variability may be explained by the funneling of the seismic waves and the controlling their polarization through the seismic waveguide. On the other hand, the southwestern basin edge exhibits an increase in ground motion variability. Seismic waves travel directly from bedrock to the basin edge; the MeSO-net sites are closer to the fault. We interpret that in that case, the close basin edge is responsibly to perturb

#### 4.4. Coupling of Source Directivity and Path Effects

Source directivity is often assumed to greatly impact ground motions, in particular at long seismic periods. Denolle, Dunham, et al. (2014) showed a coupling of source directivity and basin effects for ground motions predicted in the Los Angeles Basin due to a San Andreas event. Wang and Jordan (2014) also showed that such coupling was particularly strong for certain epicentral locations, calling them “coupling points.” Here we also investigate the role of source directivity in ground motion. We find that in general, the difference in ground motions between a southward (toward Tokyo) and the northward (away from Tokyo) rupture is lower in the VEA predictions than in the synthetic examples. This reduction is more pronounced for ground motions in the northern part of the basin, and we interpret that long-range 3-D wave propagation overcomes the finite source effects in ground motions.

We estimate the median of ground motions for all sites and for all scenario sources for given epicentral locations and show these median values (PGD, PGV, and PGA) in Figure 17. We find that the directivity effect is stronger for long period (PGD) than for the high frequencies (PGA), as expected. For a given set of source parameters (distributions of rupture velocity, slip, and rise time), the bilateral ruptures experience a stronger peak moment rate that is more than twice that of the unilateral rupture (Figure 6c). In a laterally homogeneous medium and in the point-source approximation, the PGMs are proportional to the peak moment rate value and thus should exhibit a symmetry with the highest value for the bilateral ruptures. Instead, the variations in PGMs along epicentral distance reveal that

1. the amplification due to the peak moment rate function expected by the theory is reduced for VEA;
2. southward ruptures generate 1.25 greater shaking in Kanto than northward ruptures;
3. there exists a coupling point,  $S_{60}$ , that generates overall 1.7 time stronger shaking in Kanto than other ruptures;
4. the long periods are more sensitive to the location of the epicenter than the short periods.

To establish where the amplification between  $S_{60}$  and  $S_{160}$  occurs, we show the ratio of the PGDs in Figure 18. The amplification occurs at all sites and is greater in the southern part of the basin, in particular at the transition between the Sagami and Kanto basins. It is interesting to note that this amplification occurs where the

H/V ratios are the largest (Figure 8) and where the wavefield polarization is perpendicular to the basin edges (Figure 14b). Therefore, there must exist aspect in the kinematic ruptures of bilateral ruptures on the ISTL that favor the excitation of the Rayleigh wave higher mode.

## 5. Conclusions

Greater Tokyo is expected to experience the ground motions of a large rupture on the ISTL in the near future. Using the ambient seismic field, we have calculated empirically the elastodynamic Green tensor between Hi-net stations that act as virtual sources and MeSO-net stations that act as receivers. The ambient-field Green tensor exhibits a rich wavefield with multiple surface-wave modes and can be used in the VEA approach to predict long-period surface-wave amplitudes. Because only the relative amplitude is retrieved from the ambient noise deconvolution, we calibrate the relative amplitudes to the absolute level using the 22 November 2014 Northern Nagano earthquake as a calibration event. Uncertainties in ground motion that arise from this calibration are approximately a factor of 2 in the final shaking levels.

We construct 270 scenario sources for a oblique left-lateral M7.6 on the ISTL and test for ground motion levels and variability due to unknown sources. We conclude that

1. the overall linear ground motion between 1 and 10 s is elevated in the Kanto Basin ( $PGD = 20$  cm,  $PGV = 50$  cm/s,  $PGA = 74$  cm/s<sup>2</sup> = 0.07 g, and  $SA$  [at 3 s] = 1.55 m/s<sup>2</sup> = 15% g), values that approach the elastic-plastic threshold;
2. the ground motions are greater in the central and southern parts of Kanto Basin;
3. the H/V ratios are about 2.5, slightly greater than predicted by simple Earth structure, and particularly elevated in the southern part of the basin (up to 80);
4. ground motion variability due to uncertainty in scenario sources is particularly affected by the crustal structure; it is reduced in the northern part of the basin and enhanced in the southern part;
5. basin amplification is greater for the horizontal than for the vertical ground motion;
6. the dominant polarization of horizontal waves varies smoothly across Kanto due to basin structure;
7. bilateral ruptures can produce greater shaking than unilateral ruptures with a factor up to 1.7 for epicenters located at the coupling point.

The southern H/V ratios are high (up to 80), ground motion variability is larger by 50%, horizontal seismic amplification due to 3-D path effects is greater, the horizontal wavefield is dominantly oriented perpendicular to the basin edge, and the sensitivity to directivity coupling is strong. For identical characterization of the seismic wavefield, the wave propagation in the northern part of the Kanto Basin has opposed to that in the southern part. In all parts of the basin, the basin shape affects the ground motion.

Overall, this investigation confirms the importance of shallow crustal structure in controlling ground motion. It amplifies seismic waves where the basin is deep; it reduces the vertical component variability but aggravates the variability of the horizontal components. Because of a coupling between wave propagation and earthquake source, our results further validate that rupture initiation and propagation controls ground shaking amplitude and variability in Kanto for future ISTL large earthquakes.

## References

- Adda-Bedia, M., & Madariaga, R. (2008). Seismic radiation from a kink on an antiplane fault. *Bulletin of the Seismological Society of America*, 98(5), 2291–2302.
- Afnimar, Koketsu, K., & Komazawa, M. (2003). 3-D Structure of the Kanto basin, Japan from Joint Inversion of Refraction and Gravity Data, *IUGG 2003 Scientific program and abstracts*. edited by IUGG, pp. SS04/07A/A03–002, B.487.
- Aki, K., & Richards, P. G. (2002). *Quantitative seismology* (2nd ed.). Sausalito, CA: University Science Books.
- Aochi, H., & Madariaga, R. (2003). The 1999 Izmit, Turkey, earthquake: Nonplanar fault structure, dynamic rupture process, and strong ground motion. *Bulletin of the Seismological Society of America*, 93(3), 1249–1266.
- Aochi, H., & Ulrich, T. (2015). A probable earthquake scenario near Istanbul determined from dynamic simulations. *Bulletin of the Seismological Society of America*, 103(3), 1468–1475.
- Archuleta, R. J., & Ji, C. (2016). Moment rate scaling for earthquakes 3.3–5.3 with implications for stress drop. *Geophysical Research Letters*, 43, 12,004–12,011. <https://doi.org/10.1002/2016GL071433>
- Baltay, A. A., Hanks, T. C., & Abrahamson, N. A. (2017). Uncertainty, variability, and earthquake physics in ground-motion prediction equations. *Bulletin of the Seismological Society of America*, 107(4), 1754–1772.
- Bard, P.-Y., & Bouchon, M. (1980). The seismic response of sediment-filled valleys. Part 2. The case of incident *P* and *SV* waves. *Bulletin of the Seismological Society of America*, 70(5), 1921–1941.
- Boatwright, J., & Choy, G. L. (1989). Acceleration spectra for subduction zone earthquakes. *Journal of Geophysical Research*, 94(B11), 15,541–15,553.

### Acknowledgments

The authors thank Shigeki Nakagawa and Yannis Panayotopoulos for their assistance with the MeSO-net data and Loïc Viens for helpful discussions. The ambient-field Green's functions are available through the Harvard Dataverse platform at <https://doi.org/10.7910/DVN/G2KFLY>. The VEA codes are available at [github.com/mdenolle/vea](https://github.com/mdenolle/vea). The synthetic surface-wave codes and kinematic sources are available at [github.com/mdenolle/gesc/kinematic](https://github.com/mdenolle/gesc/kinematic). This work was partially supported by NSF grant EAR-1520867, SCEC (proposals 15036 and 16246), by the Special Project for Reducing Vulnerability for Urban Mega Earthquake Disasters from the Ministry of Education, Culture, Sports, Science, and Technology of Japan, and by a grant from Labex OSUG@2020 (Investissements d'avenir-ANR10 LABX56). The SCEC contribution number for this paper is 7914. SCEC is funded by NSF Cooperative Agreement EAR-0529922 and USGS Cooperative Agreement 07HQAG0008.

- Boatwright, J., & Choy, G. L. (1992). Acceleration source spectra anticipated for large earthquakes in northeastern North America. *Bulletin of the Seismological Society of America*, *82*(2), 660–682.
- Boué, P., Denolle, M., Hirata, N., Nakagawa, S., & Beroza, G. C. (2016). Beyond basin resonance: Characterizing wave propagation using a dense array and the ambient seismic field. *Geophysical Journal International*, *206*(2), 1261–1272.
- Bowden, D. C., Tsai, V. C., & Lin, F.-C. (2016). Site amplification, attenuation and scattering from noise correlation amplitudes across a dense array in Long Beach, CA. *Geophysical Research Letters*, *43*, 1360–1367. <https://doi.org/10.1002/2014GL026662>
- Campbell, K. W., & Bozorgnia, Y. (2014). NGA-West2 ground motion models for the average horizontal components of PGA, PGV, and 5% damped linear acceleration response spectra. *Earthquake Spectra*, *30*(3), 1087–1115.
- Crempien, J. G. F., & Archuleta, R. J. (2015). UCSB method for simulation of broadband ground motion from kinematic earthquake sources. *Seismological Research Letters*, *86*(1), 61–67.
- Cruz-Atienza, V. M., Tago, J., Sanabria-Gómez, J., Chaljub, E., Etienne, V., Virieux, J., & Quintanar, L. (2016). Long duration of ground motion in the paradigmatic valley of Mexico. *Scientific Report*, *6*, 38807.
- Day, S. M., Roten, D., & Olsen, K. B. (2012). Adjoint analysis of the source and path sensitivities of basin-guided waves. *Geophysical Journal International*, *189*, 1103–1124.
- Denolle, M. A., Dunham, E. M., & Beroza, G. C. (2012). Solving the surface-wave eigenproblem with Chebyshev spectral collocation. *Bulletin of the Seismological Society of America*, *102*, 1214–1223. <https://doi.org/10.1785/0120110183>
- Denolle, M. A., Dunham, E. M., Prieto, G. A., & Beroza, G. C. (2013). Ground motion prediction of realistic earthquake sources using the ambient seismic field. *Journal of Geophysical Research: Solid Earth*, *118*, 2102–2118. <https://doi.org/10.1029/2012JB009603>
- Denolle, M. A., Dunham, E. M., Prieto, G. A., & Beroza, G. C. (2014). Strong ground motion prediction using virtual earthquakes. *Science*, *343*, 399–403. <https://doi.org/10.1126/science.1245678>
- Denolle, M. A., Miyake, H., Nakagawa, S., Hirata, N., & Beroza, G. C. (2014). Long-period seismic amplification in the Kanto Basin from the ambient seismic field. *Geophysical Research Letters*, *41*, 2319–2325. <https://doi.org/10.1002/2014GL059425>
- Denolle, M. A., & Shearer, P. M. (2016). New perspectives on self similarity for shallow thrust earthquakes. *Journal of Geophysical Research: Solid Earth*, *121*, 6533–6565. <https://doi.org/10.1002/2016JB013105>
- Douglas, J., & Edwards, B. (2016). Recent and future developments in earthquake ground motion estimation. *Earth-Science Reviews*, *160*, 203–219.
- Ekström, G., Nettles, M., & Dziewonski, A. M. (2012). The global CMT project 2004–2010: Centroid-moment tensors for 13,017 earthquakes. *Physics of the Earth and Planetary Interiors*, *200–201*, 1–9.
- Frankel, A. (2009). A constant stress-drop model for producing broad-band synthetic seismograms: Comparison with the next generation attenuation relations. *Bulletin of the Seismological Society of America*, *99*, 664–680.
- Fukuyama, E., & Mikumo, T. (2006). Dynamic rupture propagation during the 1891 Nobi, Central Japan, earthquake: A possible extension to the branched faults. *Bulletin of the Seismological Society of America*, *96*(4A), 1257–1266.
- Furumura, T., & Hayakawa, T. (2007). Anomalous Propagation of long-period ground motions recorded in Tokyo during the 23 October 2004 Mw 6.6 Niigata-ken Chuetsu, Japan, earthquake. *Bulletin of the Seismological Society of America*, *97*(3), 863–880.
- Graves, R., Jordan, T. H., Callaghan, S., Deelman, E., Field, E., Juve, G., et al. (2011). Cybershake: A physics-based seismic hazard model for Southern California. *Pure and Applied Geophysics*, *168*(3–4), 367–381.
- Griber, G., Liberty, L. M., Mikesell, T. D., & Michaels, P. (2016). Isolating retrograde and prograde Rayleigh-wave modes using a polarity mute. *Geophysics*, *81*(5), 379–385.
- Guatteri, M., Mai, P. M., Beroza, G. C., & Boatwright, J. (2003). Strong ground-motion prediction from stochastic-dynamic source models. *Bulletin of the Seismological Society of America*, *93*(1), 301–313.
- Heaton, T. H. (1990). Evidence for and implications of self-healing pulses of slip in earthquake rupture. *Physics of the Earth and Planetary Interiors*, *64*(1), 1–20.
- Kawase, H., & Aki, K. (1989). A study on the response of a soft basin for incident *S*, *P*, and Rayleigh waves with special reference to the long duration observed in Mexico City. *Bulletin of the Seismological Society of America*, *79*, 1361–1382.
- Koketsu, K., & Kikuchi, M. (2000). Propagation of seismic ground motion in the Kanto Basin, Japan. *Science*, *288*(5469), 1237–1239.
- Koketsu, K., Miyake, H., Afnimar, & Tanaka, Y. (2009). A proposal for a standard procedure of modeling 3-D velocity structures and its application to the Tokyo metropolitan area, Japan. *Tectonophysics*, *472*, 290–300.
- Kondo, H., Toda, S., Okumura, K., & Takada, K. (2006). Geomorphic features indicating strike-slip movement along the East Matsumoto Basin faults, Itoigawa-Shizuoka Tectonic Line active fault systems, central Japan. *Journal of Geography (in Japanese)*, *115*(2), 208–220.
- Lawrence, J. F., & Prieto, G. A. (2011). Attenuation tomography of the western United States from ambient seismic noise. *Journal of Geophysical Research*, *116*, B06302. <https://doi.org/10.1029/2010JB007836>
- Lawrence, J. F., Denolle, M. A., Seats, K. J., & Prieto, G. A. (2013). A numeric evaluation of attenuation from ambient noise correlation functions. *Journal of Geophysical Research: Solid Earth*, *118*, 6134–6145. <https://doi.org/10.1002/2012JB009513>
- Lozos, J. C. (2016). A case for historic joint rupture of the San Andreas and San Jacinto faults. *Science Advances*, *2*(3), E1500621. <https://doi.org/10.1126/sciadv.1500621>
- Ma, Y., Clayton, R., & Li, D. (2016). Higher-mode ambient-noise Rayleigh waves in sedimentary basins. *Geophysical Journal International*, *206*(3), 1634–1644.
- Mai, P. M., & Beroza, G. C. (2002). A spatial random field model to characterize complexity in earthquake slip. *Journal of Geophysical Research*, *107*(B11), 2308. <https://doi.org/10.1029/2001JB000588>
- Mai, P. M., Galis, M., Thingbaijam, K. K. S., Vyas, J. C., & Dunham, E. M. (2017). Accounting for fault roughness in pseudo-dynamic ground-motion simulations. *Pure and Applied Geophysics*, *174*, 3419–3450. <https://doi.org/10.1007/s00024-017-1536-8>
- Mikumo, T., & Ando, M. (1976). A search into the faulting mechanism of the 1891 Great Nobi earthquake. *Journal of Physics of the Earth*, *24*, 62–87.
- Miyake, H., & Koketsu, K. (2005). Long-period ground motions from a large offshore earthquake: The case of the 2004 off the Kii peninsula earthquake, Japan. *Earth, Planets and Space*, *57*, 203–207.
- Nakata, T., & Imaizumi, T. (2002). *Digital active fault map of Japan*. Tokyo: University of Tokyo Press.
- Nielsen, S., & Madariaga, R. (2003). On the self-healing fracture mode. *Bulletin of the Seismological Society of America*, *93*(6), 2375–2388.
- Okumura, K. (2001). Paleoseismology of the Itoigawa-Shizuoka tectonic line in central Japan. *Journal of Seismology*, *5*, 411–431.
- Okumura, K., Shmokawa, K., Yamazaki, H., & Tsukuda, E. (1994). Recent surface faulting events along the middle section of the Itoigawa-Shizuoka tectonic line—Trenching survey of the Gofukuji Fault near Matsumoto, central Japan. *Zisin*, *46*(425–438).
- Olsen, K., Day, S. M., Minster, J., Cui, Y., Chourasia, A., Faerman, M., et al. (2006). Strong shaking in Los Angeles expected from southern San Andreas earthquakes. *Geophysical Research Letters*, *33*, L07305. <https://doi.org/10.1029/2005GL025472>

- Olsen, K. B., Day, S. M., Dalguer, L. A., Mayhew, J., Cui, Y., Zhu, J., et al. (2009). ShakeOut-D: Ground motion estimates using an ensemble of large earthquakes on the San Andreas fault with spontaneous rupture propagation. *Geophysical Research Letters*, *36*, L04303. <https://doi.org/10.1029/2008GL036832>
- Panayotopoulos, Y., Hirata, N., Hashima, A., Iwasaki, T., Sakai, S., & Sato, H. (2016). Seismological evidence of an active footwall shortcut thrust in the northern Itoigawa-Shizuoka tectonic line derived by the aftershock sequence of the 2014 M 6.7 Northern Nagano earthquake. *Tectonophysics*, *679*(4), 15–28.
- Prieto, G. A., & Beroza, G. C. (2008). Earthquake ground motion prediction using the ambient seismic field. *Geophysical Research Letters*, *35*, L14304. <https://doi.org/10.1029/2008GL034428>
- Prieto, G. A., Denolle, M., Lawrence, J. F., & Beroza, G. C. (2011). On amplitude information carried by the ambient seismic field. *Comptes Rendus Geoscience*, *343*, 600–614. <https://doi.org/10.1016/j.crte.2011.03.006>
- Prieto, G. A., Lawrence, J. F., & Beroza, G. C. (2009). Anelastic earth structure from the coherency of the ambient seismic field. *Journal of Geophysical Research*, *114*, B07303. <https://doi.org/10.1029/2008JB006067>
- Rivet, D., Campillo, M., Sánchez-Sesma, F. J., Shapiro, N. M., & Singh, S. K. (2015). Identification of surface wave higher modes using a methodology based on seismic noise and coda waves. *Geophysical Journal International*, *203*(2), 856–868.
- Roten, D., Olsen, K. B., Day, S. M., Cui, Y., & Fäh, D. (2014). Expected seismic shaking in Los Angeles reduced by San Andreas fault zone plasticity. *Geophysical Research Letters*, *41*, 2769–2777. <https://doi.org/10.1002/2014GL059411>
- Roten, D., Olsen, K. B., Day, S. M., & Cui, Y. (2017). Quantification of fault zone plasticity effects with spontaneous rupture simulations. *Pure and Applied Geophysics*, *174*(9), 3369–3391.
- Roux, P. (2009). Passive seismic imaging with directive ambient noise: Application to surface waves and the San Andreas Fault in Parkfield, CA. *Geophysical Journal International*, *179*, 367–373.
- Sagiya, T., Nishimura, T., & Iio, Y. (2004). Heterogeneous crustal deformation along the central-northern Itoigawa-Shizuoka tectonic line fault system, central Japan. *Earth, Planets and Space*, *56*, 1247–1252.
- Sánchez-Sesma, F. J., & Campillo, M. (2006). Retrieval of the Green's function from cross correlation: The canonical elastic problems. *Bulletin of the Seismological Society of America*, *96*, 1182–1191. <https://doi.org/10.1785/0120050181>
- Sato, H. (1994). The relationship between late Cenozoic tectonic events and stress field and basin development in northeast Japan. *Journal of Geophysical Research*, *99*(B11), 22,261–22,274.
- Sato, T., Graves, R. W., & Somerville, P. G. (1990). Three-dimensional finite-difference simulations of long-period strong motions in the Tokyo metropolitan area during the 1990 Odawara earthquake ( $M_j$  5.1) and the Great 1923 Kanto earthquake ( $M_j$  8.2) in Japan. *Bulletin of the Seismological Society of America*, *89*(3), 579–607.
- Savage, M. K., Lin, F.-C., & Townend, J. (2013). Ambient noise cross-correlation observations of fundamental and higher-mode Rayleigh wave propagation governed by basement resonance. *Geophysical Research Letters*, *40*, 3556–3561. <https://doi.org/10.1002/grl.50678>
- Schmedes, J., Archuleta, R. J., & Lavallée, D. (2010). Correlation of earthquake source parameters inferred from dynamic rupture simulations. *Journal of Geophysical Research*, *115*, B03304. <https://doi.org/10.1029/2009JB006689>
- Schmedes, J., Archuleta, R. J., & Lavallée, D. (2013). A kinematic rupture model generator incorporating spatial interdependency of earthquake source parameters. *Geophysical Journal International*, *192*, 1116–1131.
- Seats, K. J., Lawrence, J. F., & Prieto, G. A. (2011). Improved ambient noise correlation functions using Welch's methods. *Geophysical Journal International*, *188*, 513–523. <https://doi.org/10.1111/j.1365-246X.2011.05263.x>
- Smith, W. H., & Sandwell, D. T. (1997). Global sea floor topography from satellite altimetry and ship depth soundings. *Science*, *277*(5334), 1956–1962.
- Stehly, L., & Boué, P. (2017). On the interpretation of the amplitude decay of noise correlations computed along a line of receivers. *Geophysical Journal International*, *209*(1), 358–372.
- Stehly, L., Campillo, M., & Shapiro, N. M. (2006). A study of the seismic noise from its long-range correlation properties. *Journal of Geophysical Research*, *111*, B10306. <https://doi.org/10.1029/2005JB004237>
- Tinti, E., Fukuyama, E., Piatanesi, A., & Cocco, M. (2005). A kinematic source-time function compatible with earthquake dynamics. *Bulletin of the Seismological Society of America*, *95*(4), 1211–1223.
- Tsai, V. C., Bowden, D. C., & Kanamori, H. (2017). Explaining extreme ground motion in Osaka Basin during the 2011 tohoku earthquake. *Geophysical Research Letters*, *44*, 7239–7244. <https://doi.org/10.1002/2017GL074120>
- Viens, L., Denolle, M. A., Miyake, H., Sakai, S., & Nakagawa, S. (2017). Retrieving impulse response function amplitudes from the ambient seismic field. *Geophysical Journal International*, *210*(1), 210–222.
- Viens, L., Koketsu, K., Miyake, H., Sakai, S., & Nakagawa, S. (2016). Basin-scale Green's functions from the ambient seismic field recorded by MeSO-net stations. *Journal of Geophysical Research: Solid Earth*, *121*, 2507–2520. <https://doi.org/10.1002/2016JB012796>
- Villani, M., & Abrahamson, N. A. (2015). Repeatable site and path effects in the ground-motion sigma based on empirical data from southern California and simulated waveforms from the Cybersake platform. *Bulletin of the Seismological Society of America*, *106*(5), 2681–2695.
- Wang, F., & Jordan, T. H. (2014). Comparison of probabilistic seismic-hazard models using averaging-based factorization. *Bulletin of the Seismological Society of America*, *104*(3), 1230–1257.
- Yao, H., Campman, X., de Hoop, M. V., & van der Hilst, R. D. (2009). Estimation of surface wave Green's functions from correlation of direct waves, coda waves and ambient noise in SE Tibet. *Physics of the Earth and Planetary Interiors*, *177*(1–2), 1–11.